nature neuroscience

RESOURCE

https://doi.org/10.1038/s41593-021-00874-w

A large-scale nanoscopy and biochemistry analysis of postsynaptic dendritic spines

Martin S. Helm[1,2,3], Tal M. Dankovich[2,3,4], Sunit Mandad[3], Burkhard Rammner[3], Sebastian Jähne[2,3,4], Vanessa Salimi[3], Christina Koerbs[3], Richard Leibrandt[5], Henning Urlaub[6,7], Thomas Schikorski[8] and Silvio O. Rizzoli[3,9] ✉

Dendritic spines, the postsynaptic compartments of excitatory neurotransmission, have different shapes classified from 'stubby' to 'mushroom-like'. Whereas mushroom spines are essential for adult brain function, stubby spines disappear during brain maturation. It is still unclear whether and how they differ in protein composition. To address this, we combined electron microscopy and quantitative biochemistry with super-resolution microscopy to annotate more than 47,000 spines for more than 100 synaptic targets. Surprisingly, mushroom and stubby spines have similar average protein copy numbers and topologies. However, an analysis of the correlation of each protein to the postsynaptic density mass, used as a marker of synaptic strength, showed substantially more significant results for the mushroom spines. Secretion and trafficking proteins correlated particularly poorly to the strength of stubby spines. This suggests that stubby spines are less likely to adequately respond to dynamic changes in synaptic transmission than mushroom spines, which possibly explains their loss during brain maturation.

Dendritic spines are the most important postsynaptic compartment of excitatory neurons in the brain and are essential for synaptic transmission and plasticity[1–3]. They come in a variety of shapes, including the prototypical mushroom-shaped spine (a large head connected to the dendritic shaft by a thin neck), thin spines (lacking a bona fide head structure) and stubby spines (which are connected to the dendritic shaft by a very wide neck)[2,4]. Stubby spines are thought to represent an immature type, as they tend to disappear during development[5,6], while mushroom spines are the ones responsible for information transmission and learning in the adult[2,4]. Spine morphology has long been linked to synaptic function. For example, the presence of the spine neck is well known to influence synaptic function by compartmentalizing the receptor-containing spine head, thereby influencing local signaling cascades[7–9]. Moreover, the spatial organization of the postsynaptic density (PSD) and the patterning of neurotransmitter receptors are functionally relevant[10,11]. Nevertheless, our understanding of the detailed organization of spines is still limited, and there is no clear information on whether the different spine classes are fundamentally different in composition. Two scenarios could be envisioned to explain the differences between the mushroom and stubby spines. First, the amounts or positions of specific components may be widely different (Fig. 1a). This would point to the inability of stubby spines to maintain certain organelles or proteins, which would then render them less well fitted for function in the adult brain. Second, the two spine classes may be similar on average, but the composition of the stubby spines may be less well balanced, for example, more variable in relation to synaptic strength (Fig. 1b).

This is difficult to test owing to technical challenges, as spines are small and difficult to image by diffraction-limited approaches, are impossible to purify as whole spines (and not just as purified PSDs) and have a high protein density, which makes immunostaining difficult. Here, we circumvented these difficulties by imaging at super-resolution more than 100 proteins in dendritic spines, spanning many important protein classes. We found that the two spine classes are very similar on average, but that the composition of the mushroom spines correlates much more strongly to synaptic strength.

Results

A description of the neuronal cultures used. We relied on cultured hippocampal neurons, which have abundant levels of both stubby and mushroom spines[12] and are a standard model for synaptic function investigations. To analyze both the copy numbers and the locations of different proteins in the spines, we used an integrative approach (Extended Data Fig. 1), in which we combined the following techniques: (1) electron microscopy (EM) to determine the shapes, volumes and organelle distributions of the spines; (2) stimulated emission depletion (STED) microscopy to estimate the location of the proteins and to determine differences in protein amounts between different spine types; and (3) mass spectrometry (MS) to measure the protein copy numbers per cell, followed by fluorescence microscopy to transform these into copy numbers per spine (in a procedure explained in detail below). All of these measurements then converged to build quantitative three-dimensional (3D) models of average stubby and mushroom spines (Extended Data Fig. 1). We used a sandwich culture system, which enabled us to isolate neurons from glia, as required for biochemical analysis, and is easily accessible to microscopy[13]. These cultures were virtually free of glia cells and contained mainly glutamatergic neurons, with a small percentage of GABAergic ones (Extended Data Fig. 2).

[1]International Max-Planck Research School Molecular Biology, Göttingen, Germany. [2]Göttingen Graduate Center for Neurosciences Biophysics, and Molecular Biosciences, Göttingen, Germany. [3]Department for Neuro- and Sensory Physiology, University Medical Center Göttingen, Göttingen, Germany. [4]International Max-Planck Research School Neuroscience, Göttingen, Germany. [5]Data Analytics and Machine Learning Group, Department of Informatics, Technical University of Munich, Munich, Germany. [6]Department of Clinical Chemistry, University Medical Center Göttingen, Göttingen, Germany. [7]Bioanalytical Mass Spectrometry Group, Max-Planck Institute of Biophysical Chemistry, Göttingen, Germany. [8]Department of Neuroscience, Universidad Central del Caribe, Bayamon, Puerto Rico, USA. [9]Center for Biostructural Imaging of Neurodegeneration, BIN, Göttingen, Germany. ✉e-mail: srizzol@gwdg.de

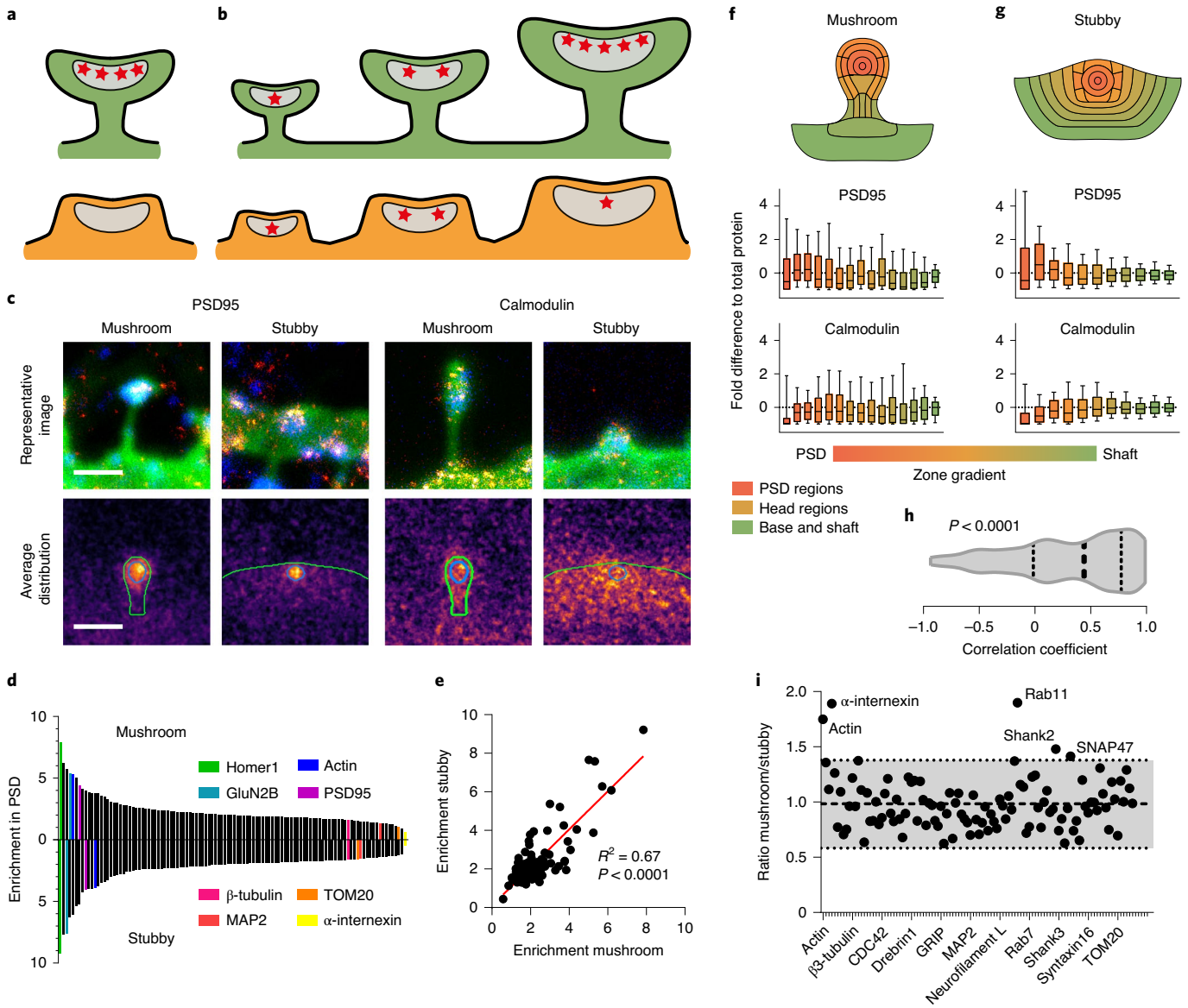

Fig. 1 | Super-resolution imaging suggests strong similarities between mushroom and stubby spines on average. a, A simple model differentiating stubby and mushroom synapses. Specific proteins of interest are present in only one of the spine classes. **b**, A more complex model, in which proteins of interest are present in both spine classes but are not correlated well to synaptic strength in one of the classes (here, stubby). **c**, Typical images of mushroom and stubby spines, in which PSD95 (left) or calmodulin (right) were analyzed. The plasma membrane is visualized (green) by the lipid dye DiO (sparsely applied so that the presynaptic neuron is not labeled and therefore does not interfere with the analysis). The PSD is visualized by immunostaining for Homer1 (blue). The proteins of interest are shown in a 'red hot' color map. The bottom panels show the average distributions of the proteins, over 123 to 226 synapses, using the inferno color map. The green lines provide rough outlines of the spines, while the blue lines indicate the margins of the PSD area. Scale bar, 500 nm. **d**, We analyzed enrichment in the PSD area for all the proteins that we studied and organized them from highest to lowest. **e**, Same as in **d**, organized as a scatter plot. Highly enriched proteins in the mushroom spines are similarly enriched in stubby spines (two-sided *F*-test, $P < 0.0001$). **f**,**g**, We separated the space of the mushroom (**f**) or the stubby (**g**) spine into different zones, from the center of the PSD to the dendritic shaft, and analyzed the enrichment or de-enrichment of each protein in each zone (expressed as the fold difference to an average of all proteins, 'total protein'). The provided examples indicate that the overall distributions of the proteins, across the zones, are similar for mushroom and stubby spines. Whiskers show 10th to 90th percentiles, the box shows quartiles and median; calmodulin, $n = 150$ (mushroom) and 140 (stubby) synapses; PSD95, $n = 226$ (mushroom) and 123 (stubby) synapses. **h**, A violin plot of the similarity of the distributions. The majority of the proteins show similar distributions in spite of the differences in spine shape (one-sample Wilcoxon test against median of 0). **i**, Ratio between the signal intensity (as a proxy for the protein copy numbers) in mushroom and stubby spines. The dashed line is the mean ratio and the gray area indicates the mean measurement error (s.e.m.) averaged across all proteins. The proteins are arranged alphabetically (only a few names are shown). For information on the sample size for each protein, please refer to Supplementary Table 5.

EM shows similarity between spine types. We started by characterizing the spine morphology by serial-section EM, analyzing 30 mushroom spines and 34 stubby spines, based on 3D reconstructions (Extended Data Fig. 3a). We focused only on these two classes as thin spines were not sufficiently frequent in our cultures. Limited differences were found between spine classes in their

underlying volume, surface and PSD size, and there were virtually no differences in the distribution and size of the different organelles (albeit the latter tended to be variable across both spine types; Extended Data Fig. 3b-d). These results are similar to previous observations of dendrites from the young brain, of an age similar to that of our cultures[5]. We validated this finding by comparing a large dataset of spines imaged with fluorescence microscopy, where even advanced clustering methods such as Gauss shift could not distinguish between the morphological characteristics of the different spines (other than the presence of the neck; Extended Data Fig. 3e,f).

An analysis of protein distributions in spines. To analyze protein distributions, we generated a scalable workflow that could be applied to very large numbers of spine and targets. This workflow addressed problems in spine immunostaining by incorporating state-of-the-art fixation and staining procedures[14] and relying on carefully validated antibodies (Supplementary Table 1). These steps were followed by standardized super-resolution microscopy, expert-curated image annotation and fully automatized image analysis. Using this approach, we were able to study the nanoscale topology of 110 proteins in relation to the membrane and the PSD positions in stubby and mushroom spines, including PSD components such as Homer, Shank, PSD95 and PSD93, glutamate receptors, major signaling proteins such as calmodulin and CaMKII, as well as trafficking molecules including SNAREs, Rabs and endocytosis cofactors (Fig. 1c and Supplementary Table 2; see Fig. 2 for the image analysis workflow and Fig. 3 for a comparison of the protein signals to the background). We found that the average organization of the proteins was remarkably similar between spine classes. Their general enrichment in the PSD area was very much alike for mushroom and stubby spines (Fig. 1d,e). Even though the spine classes were manually determined by expert users, the classification was in line with several published workflows and fulfilled general classification criteria (Extended Data Fig. 4).

A detailed analysis of their localization in the spine volume, based on dividing the volumes into arbitrarily defined zones, did not reveal major differences (Fig. 1f–g). For the latter analysis, we defined corresponding functional zones for both classes, taking into account the different spine shapes, and correlated these zones (Fig. 1h, Extended Data Fig. 5 and Supplementary Table 2). We also replicated the finding that mushroom spines had occasionally several PSD nanomodules[15], and found that the same was true for stubby spines (Extended Data Fig. 6). Finally, these experiments also enabled a comparison of the staining intensity of the different proteins among the mushroom and stubby spines by simply comparing the average signal intensities. Most average signals were relatively similar, especially when taking into account the measurement variability (Fig. 1i). Overall, this implies that the average protein distribution is similar between mushroom and stubby spines (within the resolution allowed by the STED technique and by the use of antibodies as imaging probes).

Determination of spine protein copy numbers. To correlate this analysis with the respective protein copy numbers, we developed a two-step process that circumvents the problem that spines cannot be biochemically fractionated. First, we determined the average proteome of a whole neuron, relying on quantitative MS (and, to a limited extent, to blotting; Extended Data Fig. 7a–c), which enabled the quantification of more than 6,000 proteins in absolute terms (Extended Data Fig. 7d,e). The obtained copy numbers per neuron matched well with the expected stoichiometries of several obligate protein complexes and with the relative copy numbers of several known synaptic proteins (Extended Data Fig. 8a–f). To then determine the fraction of the proteins found in spines, we immunostained the 110 proteins of interest and quantified the amount that colocalized with spines by conventional fluorescence microscopy. This provided an estimate for the total fraction of the respective proteins found in spines. Knowing the spine numbers (~300 per neuron, which was obtained from imaging experiments presented in Extended Data Fig. 9a–f; see also ref. [16]) then enabled us to estimate the average copy numbers per spine for the 110 proteins (Fig. 4a,b and Supplementary Table 2). As this procedure has multiple steps, from MS to imaging, we included several control proteins in the analysis, expecting them to be present at very low levels in the spines. This was indeed the case for voltage-gated sodium channels such as $Na_v1.3$, for the inhibitory interneuron marker parvalbumin (found at variable trace levels), for the potassium channel $K_v2.1$, which is located in dendrites at GABAergic synapses, and for presynaptic markers such as synaptophysin and the vesicular acetylcholine transporter (not found in the spines at all). Finally, we would like to point out that this procedure provides average copy numbers per spine, even for proteins known to be present preferentially in a subset of spines (as proteins present in dense-core vesicles).

Knowing the numbers of stubby and mushroom synapses present in our cultures (derived from the imaging experiments shown in Fig. 1) and the ratio between the protein amounts in the different spines (Fig. 1i), we could then calculate the protein amounts specific to mushroom and stubby spines. In accordance with the findings presented in Fig. 1, the copy numbers were similar (Fig. 4c), which was also true when comparing them to all "other" spines, a heterogeneous population of all spines that could not clearly be assigned as mushroom or stubby (Fig. 4c and Extended Data Fig. 8g). We also investigated whether subclasses of spines, based on size and other morphological characteristics, show particular protein enrichment, and we found no striking differences (Extended Data Fig. 10 and Supplementary Table 3; see Supplementary Table 6 for estimates of

Fig. 2 | Image analysis workflow. a, Three-color confocal images were acquired for the protein of interest (POI; red), the PSD marker Homer1 (blue) and the membrane dye DiO (green). A STED image of the POI was subsequently acquired and aligned with the Homer1 and DiO images, using its corresponding confocal image. Synaptic puncta were then automatically identified by thresholding the Homer1 channel, and 3 × 3-µm subimages, centered on the individual Homer1 spots, were extracted for further analysis. The subimages were successively displayed in a custom-made graphical user interface, where an expert user assigned a classification ('mushroom', 'stubby' or 'other') and manually annotated the boundaries of the spine head. The user additionally determined a rectangular region in the adjacent dendritic shaft and sketched a freehand curve along the neck (for mushroom-type spines). These boundaries were then used to rotate the subimages to a similar orientation (such that the spine is pointing upwards). The images were further filtered using the DiO channel as a mask, to remove any fluorescence from outside of the synapse, and underwent median filtering (2 × 2 pixels) and background subtraction. **b**, The aligned subimages in the STED channel were pooled for each POI and used for a number of analyses as follows. 'Averaged' image of POI*:* the images were averaged to obtain a representative image of the POI distribution at spines. Intensity by zone: the dendritic region was separated into zones, as described in Fig. 1 and Extended Data Fig. 5. The fluorescence intensity was calculated for each zone (normalized by the zone area) as a percentage of the total fluorescence intensity in the spine. Zone-enrichment analysis: the enrichment by zone was calculated as the fold-average of this POI against the average fluorescence intensity determined by pooling all POIs together (labeled 'total protein' in the figures). Additional spatial analyses*:* the images were automatically segmented with a wavelet-transform-based algorithm. The detected spots and the manually annotated boundaries of the spines were used to perform various spatial analyses (Methods). For information on the sample size for each protein, please refer to Supplementary Table 5.

the total and individual protein amounts across different spine types and sizes and Extended Data Fig. 9g for estimates on their variability among experiments).

Correlation of protein amounts to synaptic strength. Having thoroughly tested the hypothesis that the average spine composition is similar between the two classes, we went on to test whether their spine make-ups may be different in relation to synaptic strength. Our spine database, consisting of more than 47,000 expert-annotated spines, enabled this analysis, and we used the PSD size (intensity of the Homer1 signal) as a proxy for synaptic strength[1]. For every protein, we calculated the correlation between its own abundance in the spine (fluorescence signal) and the Homer1 signal in both stubby and mushroom spines (Fig. 5a,b). It became rapidly obvious that the correlations were stronger and more significant for mushroom spines (Fig. 5a–c), even for proteins not thought to be part of

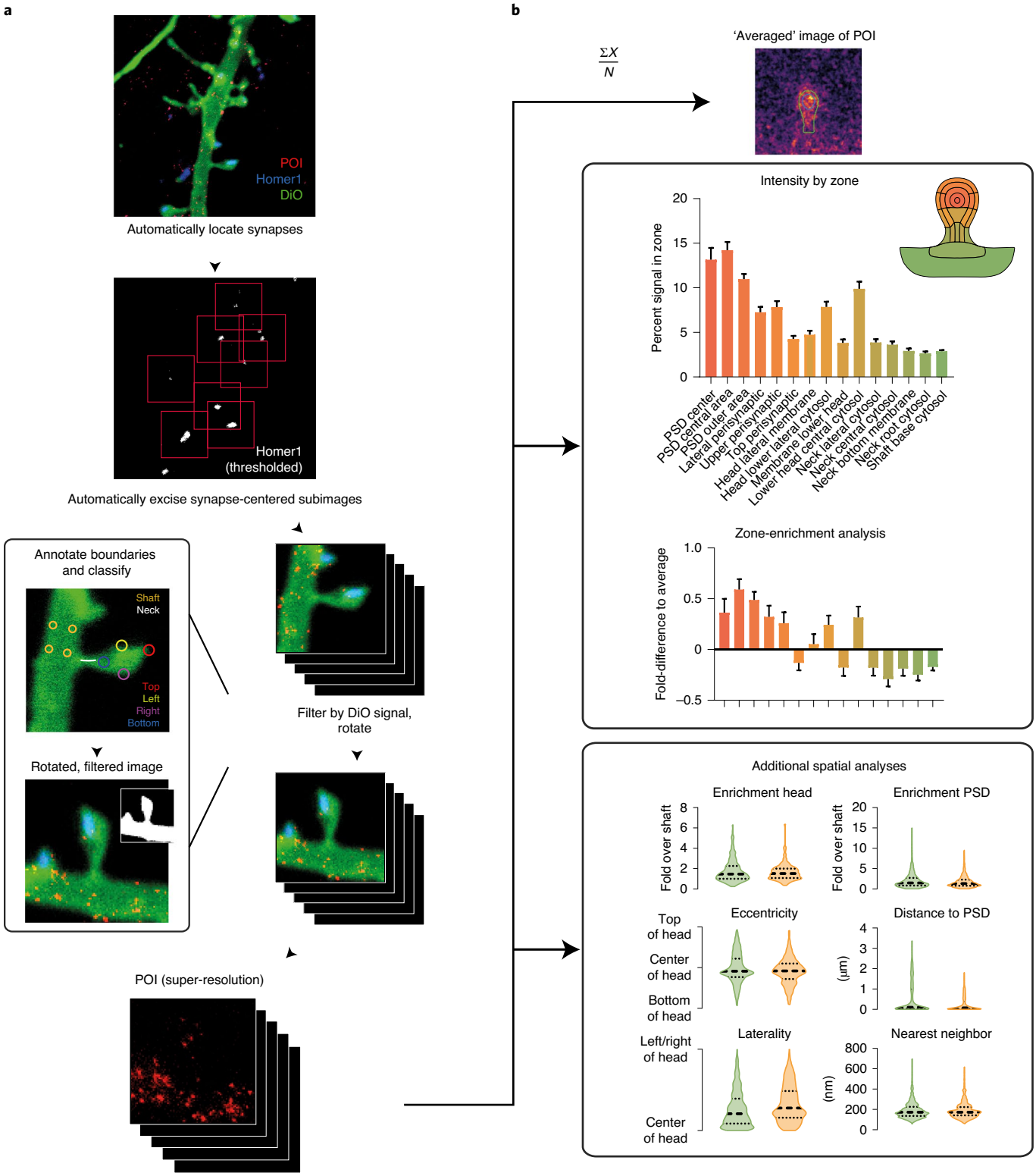

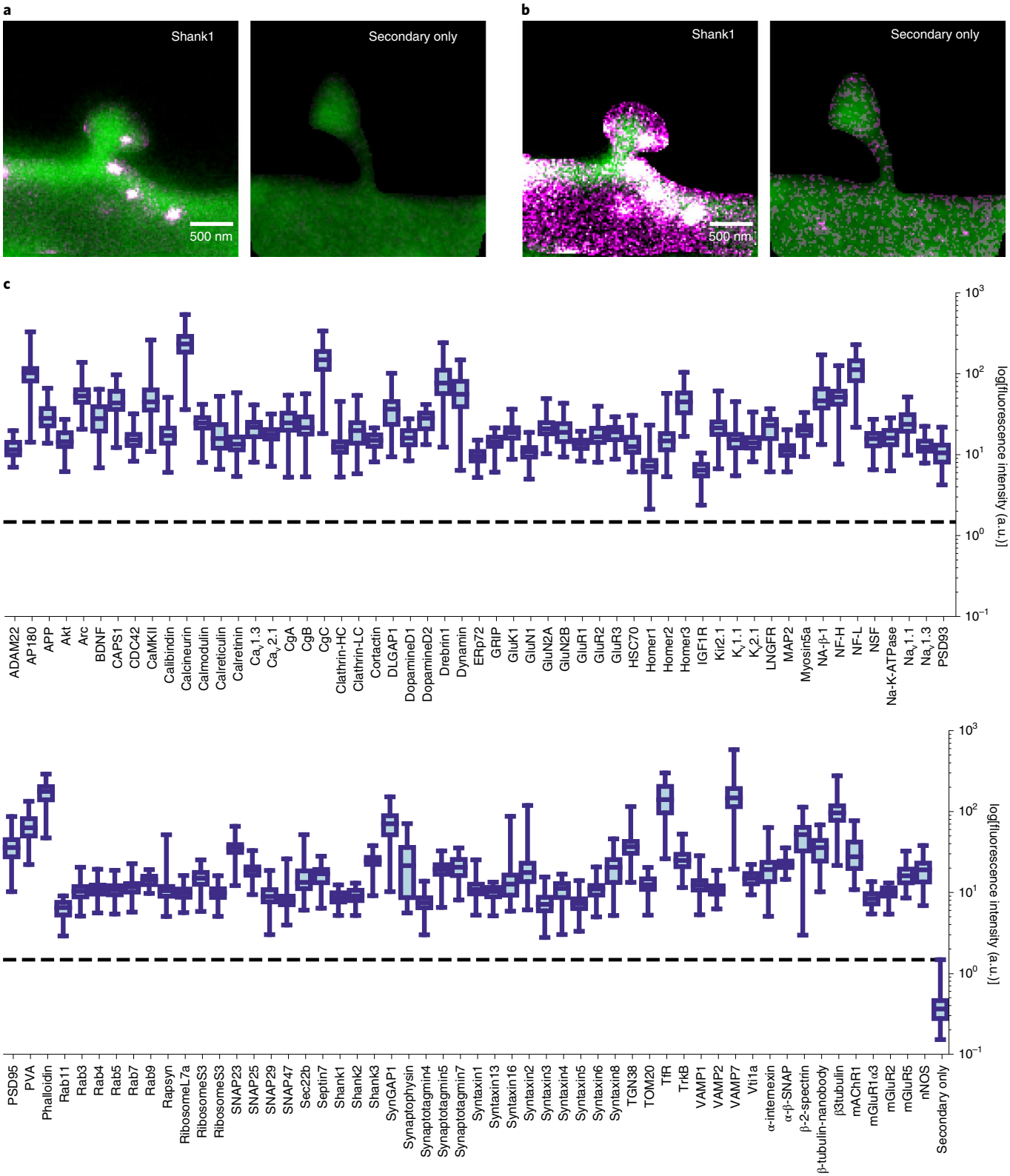

Fig. 3 | Comparison of immunofluorescence signals to background. We performed immunostainings and imaged these as described in the Methods with or without the inclusion of a primary antibody. **a**, Overlay of DiO (green; confocal) and STED images (magenta) of Shank1 (left) or secondary antibody only (right). **b**, The scaling of the images in **a** is enhanced to show the background signal in the 'secondary only' condition. **c**, We compared the intensity of the background signal (top) to the intensities of the stainings for the different proteins used here. The plot uses a log scale. The boxes indicate the median and quartiles, the whiskers indicate minimum and maximum values. The spine intensities for all proteins were significantly different from those of the 'secondary only' condition (***$P < 0.001$, Kruskal–Wallis test, followed by two-sided Mann–Whitney post-hoc tests with Bonferroni correction for multiple comparisons). For sample sizes, please refer to Supplementary Table 5.

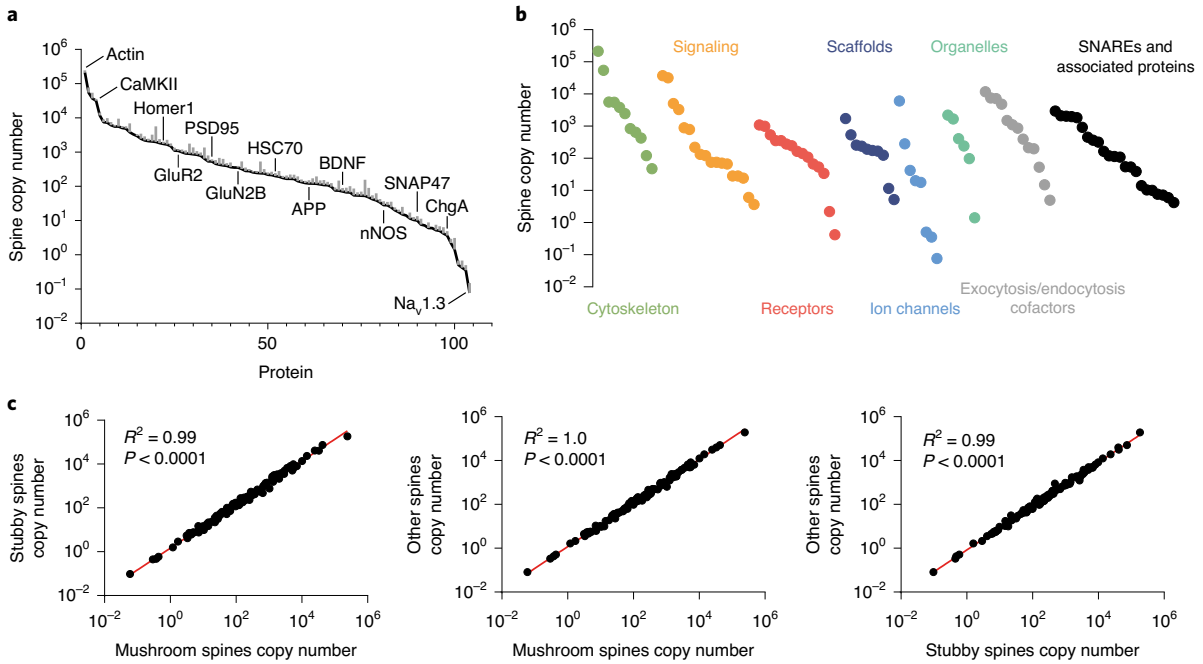

Fig. 4 | Different spines classes have similar average protein copy numbers. a, Overview of the average spine copy numbers for 110 proteins (Supplementary Table 2). **b**, Copy numbers for different protein categories. Cytoskeletal proteins and signaling molecules are the most numerous, while ion channels and receptors are the least abundant. **c**, Scatter plots comparing the protein copy numbers in different spine classes, without any normalization. Extremely high correlations were found (two-sided *F*-test).

the canonical spine proteome, such as membrane SNAREs, various ion channels, endocytosis cofactors and many cytoskeletal proteins (Fig. 5d). This difference was especially strong for proteins involved in signaling and trafficking, including Rabs, signaling enzymes, secretory proteins and ribosomes (Fig. 5e).

Overall, this implies that the proteome of stubby spines is less well associated with synaptic strength. The strong difference seen especially for trafficking proteins implies that stubby spines are less able to respond to changes in synaptic transmission by rapidly adapting their proteomes, on a time scale of minutes or hours, through local protein synthesis or trafficking. That is, they will not have the optimal amounts of all of the proteins needed for such processes on hand, unlike the mushroom spines. This offers a plausible explanation for the preference of the adult brain for the latter spine type, since spines that are expected to last many months need to be able to accurately respond to frequent changes in synaptic demands[17,18].

Homeostatic changes in the two main spine types. Several forms of synaptic plasticity have been studied since the 1970s, including mechanisms such as long-term potentiation, long-term depression and homeostatic plasticity[1–3]. These mechanisms involve changes in the activity patterns of the spines, either acutely, lasting only seconds or minutes, or chronically, lasting for hours and days. The activity changes induce remodeling of the spines, including changes in the PSD, in the receptor organization and in the spine sizes[1–3].

It has long been thought that spines remain relatively stable in the absence of such changes in activity. However, this does not appear to be the case, as spines also spontaneously remodel both in culture and in vivo[19]. Such dynamics have been difficult to observe until the introduction of super-resolution imaging for brain slices[20,21] and living brains[22,23]. The super-resolution studies showed that the majority of the spines change their morphology and PSD organization on time scales from a few minutes to 1 h, not only in cultures and cultured slices but also in adult mice[23,24]. Such changes clearly involve strong remodeling and would necessarily rely on trafficking molecules. As mushroom spines appear to have well-organized trafficking machineries (see above), they would be able to perform such rapid remodeling in an efficient manner. This is in full agreement with the in vivo observations, since the wide majority of the spines are of the mushroom type in the adult brain, which implies that virtually all of the rapidly remodeling spines observed in previous in vivo studies[23,24] are mushroom spines.

Our observations imply that stubby spines would not be able to perform such changes as efficiently, since their trafficking machineries are not well organized. However, this does not answer the question of whether and how such spines would respond to treatments that induce longer-lasting plasticity changes. In principle, even an inefficient trafficking machinery should be able to respond to changes that take place over days, as in the case of homeostatic plasticity. To test this, we induced homeostatic scaling by either silencing the cultures with tetrodotoxin (TTX) or overactivating them with bicuculline for 3 days[17,25]. Both mushroom and stubby spines were affected by these treatments (Fig. 6), which suggests that both spine types can adjust their proteomes when challenged by long-activity-changing treatments. This finding also suggests that stubby spines are sufficiently plastic to respond to the needs of the developing embryonic brain, even though they are no longer preferred in the adult.

Importantly, spine tubulin did not seem to be affected by the treatments (Fig. 6). This implies that not every protein is affected by chronic silencing or by chronic activation. These observations are in line with proteomics studies dedicated to homeostatic plasticity. One study[17] detected ~300 proteins whose regulation was different after upscaling or downscaling over 2 days. These proteins included ionotropic glutamate receptors and several trafficking proteins involved in exocytosis, GTPase function and other related processes[17], which is in good agreement with our observations. A further analysis[18] found that the protein secretion cascades involved in upscaling and downscaling are more complex than initially thought, since the proteins whose secretion changed during the first

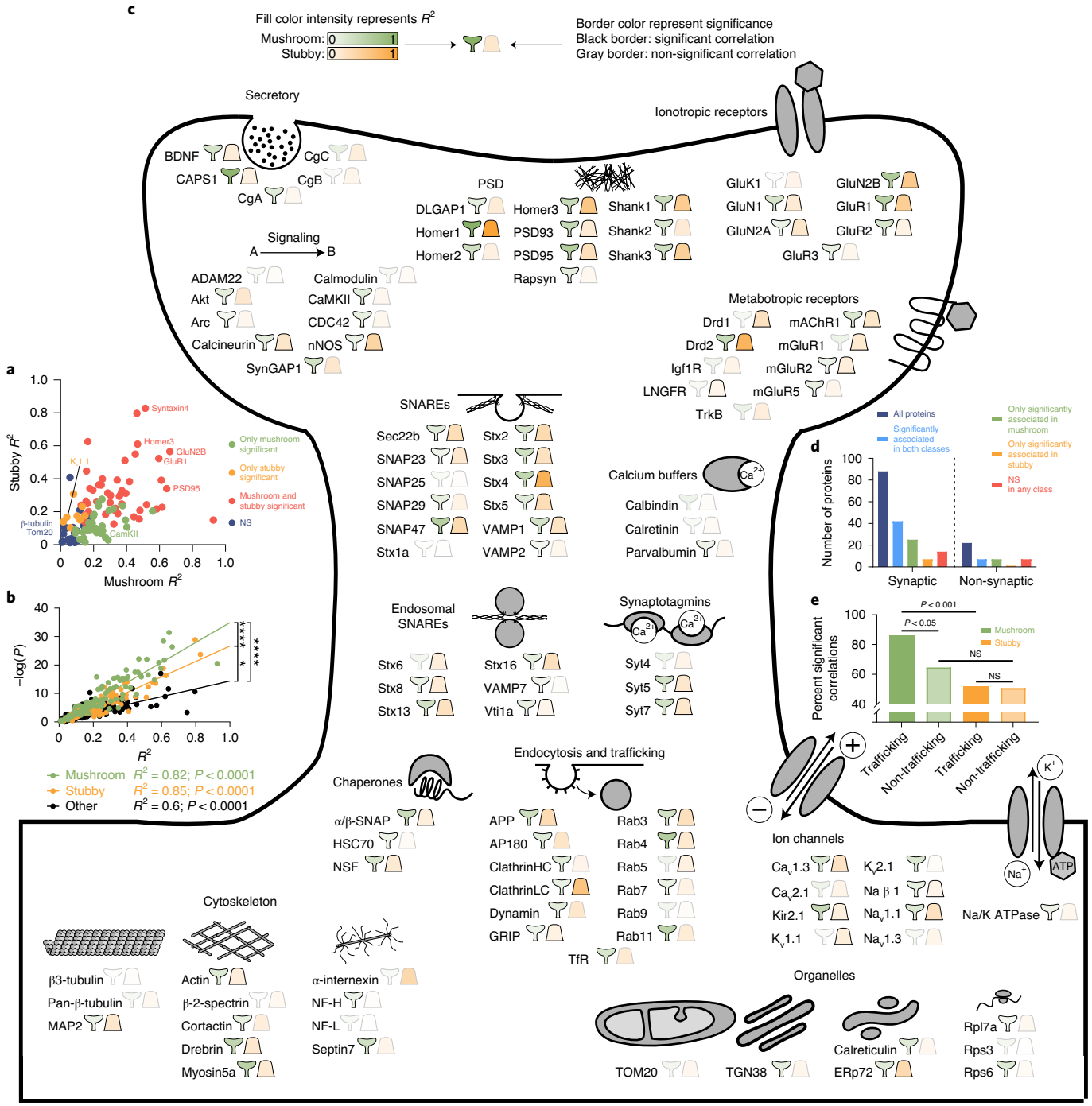

Fig. 5 | An analysis of the strength of the correlation of different proteins with the synapse strength. a, We measured the correlation of the protein amounts with the PSD mass (from the Homer1 immunostainings as shown in Fig. 1) across all spines analyzed for each individual protein. The strength of the correlations between individual protein spine intensities and PSD intensities (R^2) is reported for the mushroom and stubby spines, as a scatter plot, and the *P* value for significant correlation was Bonferroni-corrected. **b**, The significance of the correlations, as −log(*P*), is shown as a function of R^2 for mushroom, stubby and other spines. Overall, correlations are significantly stronger for mushroom spines. ****$P < 0.0001$, *$P < 0.05$; Friedman test, followed by two-sided Dunn's test. **c**, Graphical representation of the association strength of different proteins to spines. The fill color indicates the correlation strength; black borders indicate a significant correlation. Significances were verified after correcting for multiple testing, using a Bonferroni procedure. **d**, Annotation of proteins as synaptic in SynGo. Most of the proteins in this study are considered to be synaptic and correlate significantly to synaptic strength either in both mushroom and stubby spines or only in mushroom spines (left side of the graph). Note that several non-synaptic proteins also correlate significantly to synaptic strength (right side of the graph). **e**, We divided the 110 targets into trafficking proteins (including Rabs, exocytosis and endocytosis cofactors, or secretory pathway components) or non-trafficking (all others). We then counted the percentage of proteins significantly correlated with synaptic strength for trafficking and non-trafficking proteins in mushroom or stubby spines. This percentage was higher for mushroom-trafficking proteins than for all other categories, while the percentages were low in stubby spines for both trafficking and non-trafficking proteins (two-sided Mann–Whitney tests). NS, not significant.

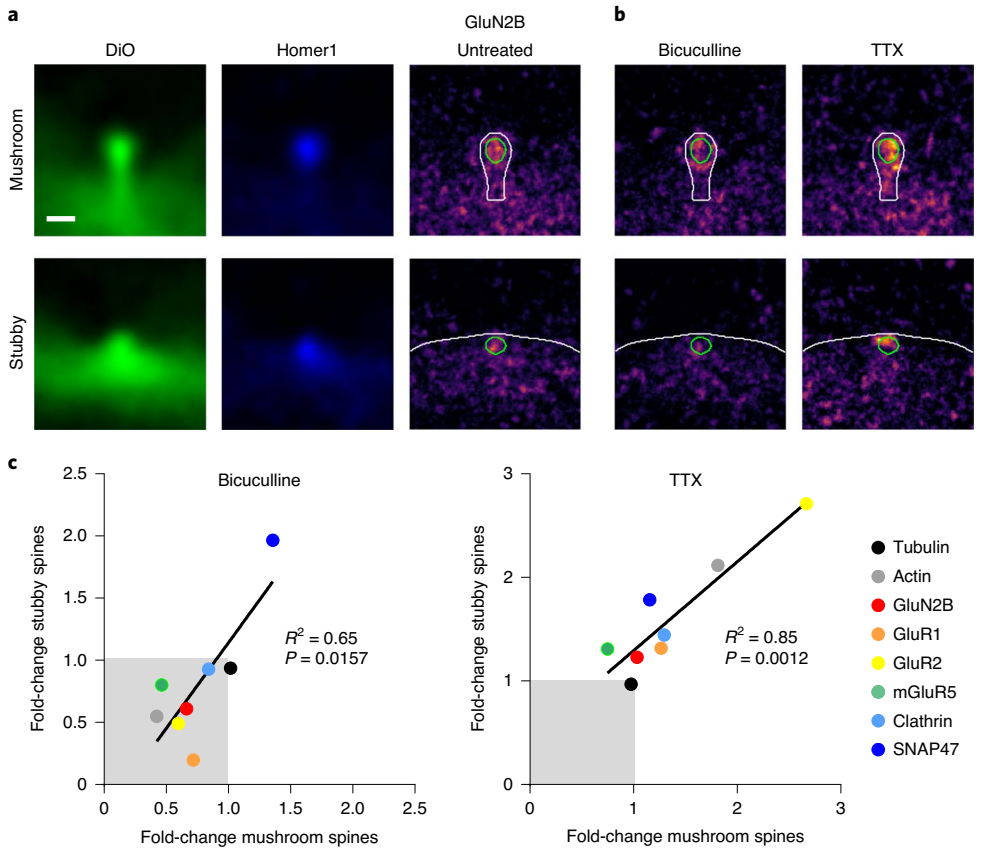

Fig. 6 | Homeostatic changes affect mushroom and stubby spines in a similar fashion. a, Dendritic spines were visualized by labeling the plasma membrane with DiO (green). The PSD was immunostained using Homer1-specific antibodies (blue). The protein of interest (here, NMDA receptors, GluN2B) is visualized in the 'inferno' color map. Averages of more than 80 control spines are shown for mushroom spines (top) and stubby spines (bottom). **b**, The hippocampal culture activity was chronically enhanced, using the $GABA_A$ receptor antagonist bicuculline, or chronically depressed, using the sodium channel blocker TTX. The images show average spine images for GluN2B for each condition (mushroom spines in the upper panels and stubby spines in the lower panels). The blur lines provide a visual indication for the rough outline of the PSD; the green lines indicate the outline of the DiO label. Scale bar, 500 nm. **c**, An analysis of the changes of eight proteins in the PSD region in the different spine types expressed as the fold-change versus the control (untreated) situation. Bicuculline reduced the amount of both AMPA and NMDA in the PSD area, while synapse silencing via TTX enhanced their amounts. Tubulin, as expected, did not substantially change in any of these conditions. The different proteins behaved similarly in the two types of spines, as indicated by the significant correlations of their fold-changes in all treatments (two-sided *F*-test). For easy visualization, the gray area indicates a reduction in the protein amounts in the PSD versus the control (fold-change lower than 1), while the white area corresponds to an increase in the protein amounts (fold-change higher than 1).

2 h of chronic silencing or activation overlapped little with those found to change after 2 days of treatment, albeit they belonged to similar functional groups. These observations again fit well with our hypothesis, namely that rapid spine dynamics (from minutes to 1–2 h) and long-term (chronic) changes are differently regulated.

Further analysis of spine parameters. At the same time, our large database lays the foundation for future modeling studies of dendritic spine function[26]. Taking all the data together, we were able to construct 3D quantitative models of average mushroom and stubby spines (Fig. 7). The structure of the models is based on 3D EM data (Extended Data Fig. 3). The proteins were then incorporated in the models, using the copy numbers estimated (Fig. 4) and relying on protein localization data derived from STED imaging. To transfer the STED information to the 3D EM model, we generated a transition scheme based on the zones defined in Fig. 1f–g, relying on carefully defined voxels of ~50 nm in all dimensions (Extended Data Fig. 5). The models also include information from an extensive database of publications on the different proteins (Supplementary Table 4), and form, to our knowledge, the most detailed description of any subcellular region to date (Supplementary Videos 1 and 2). These models showcase in a graphical format the high molecular crowding of the postsynapse, which is ~50% higher than that of the presynapse, and recapitulates the high protein density in the PSD (Figs. 4d and 8 and Supplementary Data 1 and 2). These models will constitute a useful resource for further studies. For example, they allowed us to map, with high resolution, the location of disordered and aggregation-prone areas in dendritic spines and we could visualize several hotspots for other protein features, where proteins are, for example, especially rich in particular secondary structures (Fig. 8). These observations are especially interesting since molecular crowding, especially for supersaturated proteins, influences brain function and dysfunction[27].

In addition, many other such considerations could be made, from ideas on exocytosis or endocytosis in the spines, to their capacity for local translation, which implies that our data should be an important resource for a variety of studies.

We first verified whether the copy numbers of clathrin might pose a bottleneck for endocytosis, as has been reported for the presynapse[28]. We used the clathrin heavy chain for these

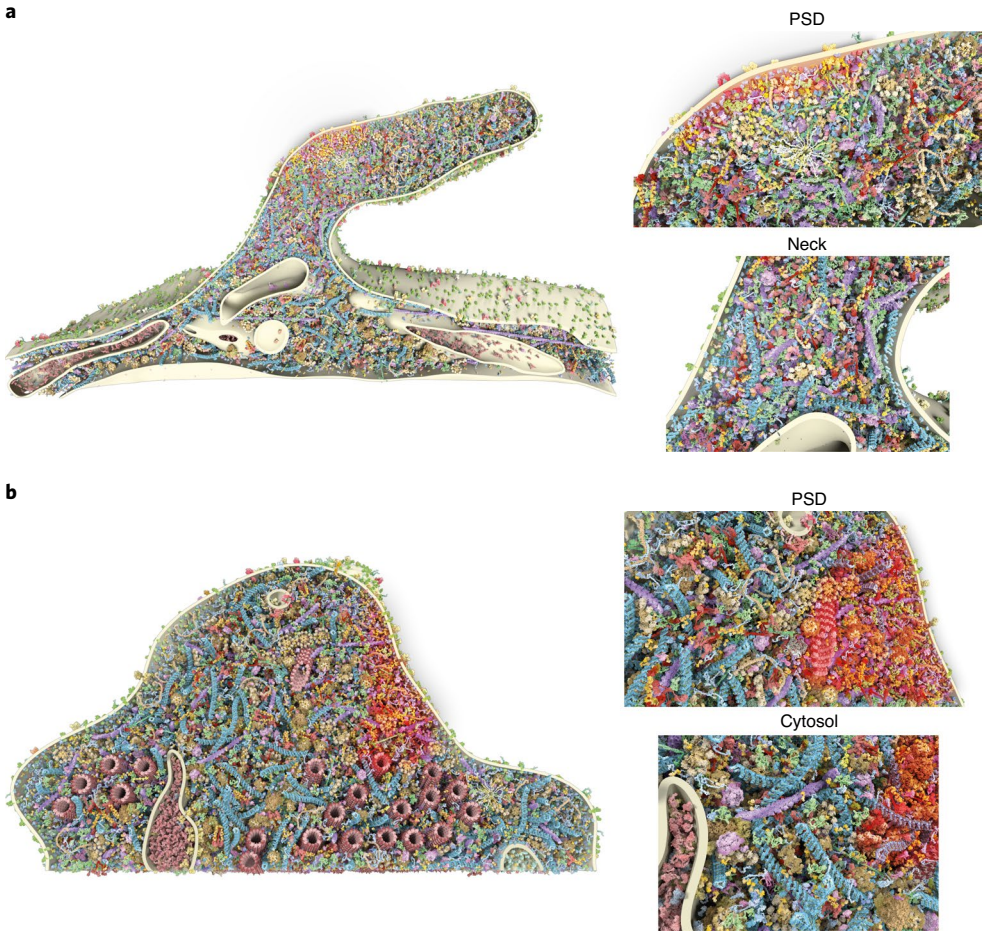

Fig. 7 | Quantitative 3D models of dendritic spines. All proteins are shown to scale, with the copy numbers and locations measured in this study and configurations according to literature. For clarity, the highly abundant monomeric actin is not shown. **a**, View into a mushroom spine. Magnifications into the PSD (highlighted with red glow) and neck are depicted. **b**, View into a stubby spine. Again, a magnification of the PSD is shown and a zoom into the cytosolic region of the spine.

calculations, for which we found relatively low copy numbers ($\text{clathrin}_{\text{total}} = 1{,}100$ per spine).

We first calculated the number of clathrin molecules found in clathrin coats already present on the plasma membrane ($\text{clathrin}_{\text{surface}}$) from the following parameters:

- The known coat radius of 50 nm (refs. [29,30]).
- The area covered by a single clathrin heavy chain of 146 nm^2 (ref. [31]).
- The fraction of the spines that contain a clathrin coat next to the PSD, of approximately 0.7 (ref. [32]).

A simple estimate result in the following:

$$\text{Clathrin}_{\text{surface}} = \frac{\text{radius}_{\text{coat}}^2 \times \pi}{\text{area}_{\text{clathrin molecule}}} \times 0.7 = 40$$

Therefore, only ~40 clathrin copies would be expected to be found on the plasma membrane near the active zone. We subtracted this number from the copy number of clathrin heavy chain molecules. We then calculated the number of vesicles that could potentially be generated by the remaining clathrin copies. Using a conservative estimate of 300 copies needed per vesicle ($\text{clathrin}_{\text{ves}}$), to be able to accommodate large vesicles[30], we calculated the maximum number of retrievable vesicles at any given time. Considering that an average endocytotic process takes 20 s ($\text{endo}_{\text{time}}$), we arrive at a maximal endocytosis rate of 10.6 events per min.

$$\text{Endo}_{\text{rate per min}} = \frac{\text{clathrin}_{\text{total}} - \text{clathrin}_{\text{surface}}}{\text{clathrin}_{\text{ves}}} \times \frac{60\ \text{s}}{\text{endo}_{\text{time}}} = 10.6 \frac{\text{events}}{\text{min}}$$

Finally, we compared this number with the endocytotic event rate that has been reported. To again take a conservative approach, we assumed that endocytosis and exocytosis are at balance in the spine and use the total number of GluA1 exocytotic events of 0.13 events per min (ref. [33]), which is almost 100 times below the maximally possible endocytosis event rate. We also performed the same calculations for dynamin, using the known number of 52 molecules needed for pinch-off[34]. This results in approximately 28.8 possible endocytosis events per min. Therefore, the number of clathrin or dynamin molecules does not appear to be limiting for endocytosis, even if other trafficking cargos or routes are also considered. We also did not find any bottlenecks for exocytosis, as the number of SNARE proteins is very high, and the number of SNARE proteins needed per fusion is substantially lower than the number of endocytotic molecules per vesicle uptake[28].

Next, we turned to the question whether the calcium buffer proteins present in our database can efficiently buffer calcium entry into the spine. We estimated the molarity of total calcium in

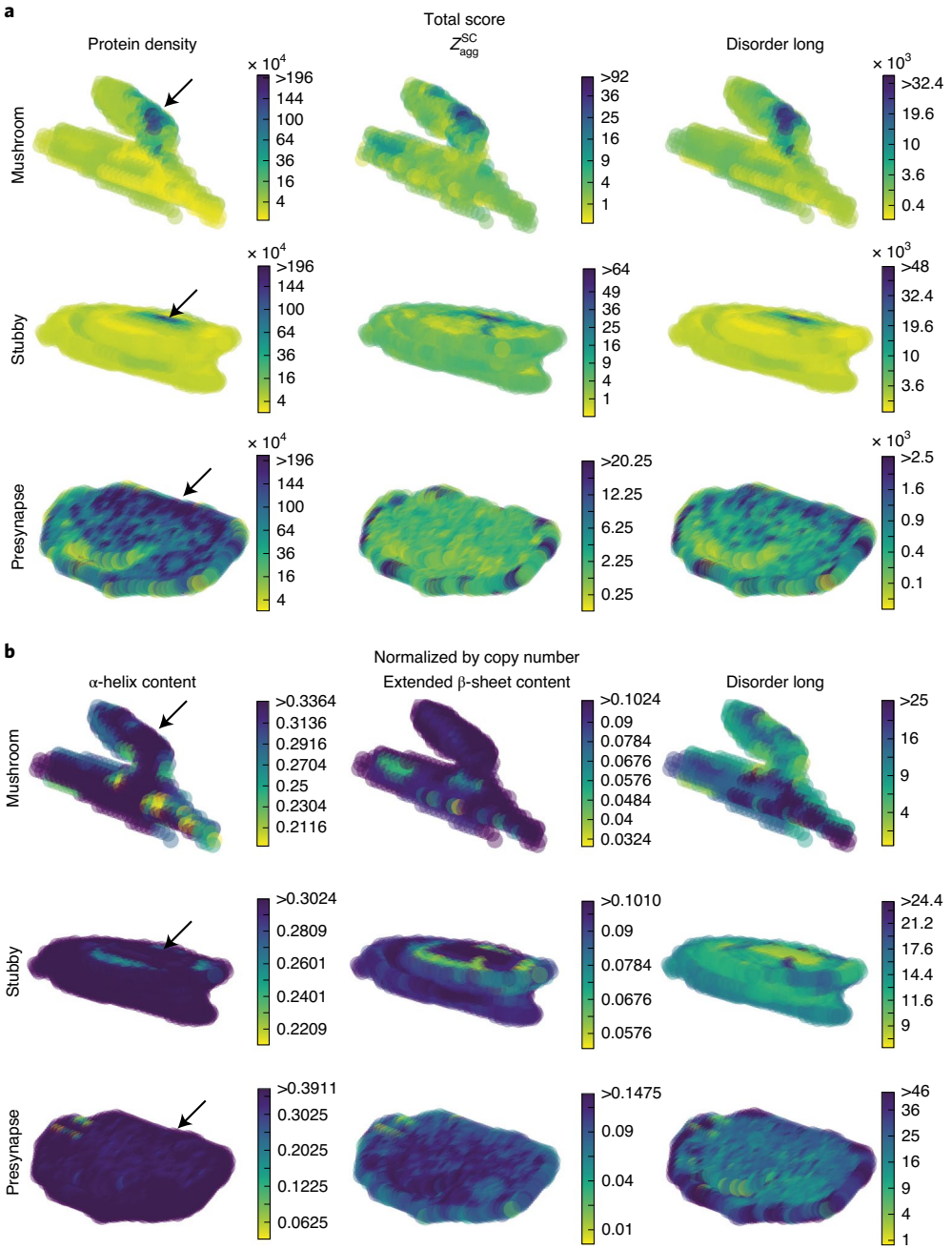

Fig. 8 | Mapping structural protein features reveals subcellular hotspots in dendritic spines. We considered a number of parameters both in postsynapse models (from the present work) and in a presynapse model[28]. The parameters include the following aspects: (1) the protein density (expressed in number of amino acids per unit space); (2) the structurally corrected aggregation propensity score (Z_{agg}^{SC})[48]; (3) the intrinsic disorder levels of the proteins (calculated in ref. [49], using the IUPred software in the "long" definition); and (4) the α-helix or β-sheet content (calculated in ref. [50]). For each parameter, we calculated either the total score for all proteins in a voxel of the 3D spine models (**a**) or the average per protein (**b**). The color map is scaled to the square root of the values and clipped at 50% of the maximum value. For clarity, only the lower half of the models is shown to enable a direct view on the PSD or active zone. The arrows indicate the PSD or active zone position. **a**, Both spine classes show an extremely high protein density in the PSD, as has been previously observed by EM. The presynapse does not exhibit a similar enrichment at the active zone. Similarly, both scores for protein disorder are enriched in the PSD. The total potential for protein aggregation is therefore the highest in the PSD. The coiled-coil content of proteins showed a similar pattern as the disorder score (not shown). In the presynapse, the only visible features are some patches on the plasma membrane, corresponding to clusters of the relatively disordered protein SNAP25. **b**, To correct for the fact that different regions of the spine have unequal protein content, we normalized the obtained feature score maps to the total protein copy number in each voxel. This revealed that, on average, the PSD contains proteins with a low disorder score, whereas the ER is enriched with proteins of high disorder, such as calreticulin. The Z_{agg}^{SC} is distributed similarly to disordered long after normalization (not shown). Notably, the ER also seems to be enriched with proteins of high α-helix content (arrowhead), whereas Golgi outposts are depleted of them. Similarly, early endosomes and LDCV- and BDNF-containing vesicles are enriched for proteins with high β-sheet content. The presynapse does not show particularly enriched or depleted regions for any of the investigated scores.

dendritic spines to be 1,000 nM, using the measured concentration of free calcium of 50 nM and a ratio of free to bound calcium of 20 (refs. [35,36]). We then calculated the molarity of each cytosolic calcium binding protein in the spine and multiplied it with its number of calcium binding sites (Supplementary Table 7). Calmodulin shows the highest calcium binding capacity by far, but even calcium buffers, such as calbindin, calcineurin and calretinin are present far in excess to bind all calcium. Therefore, efficient calcium buffering is always ensured, even during calcium influx from outside or from intracellular stores.

We performed the same analysis for calreticulin, an endoplasmic reticulum (ER)-resident calcium buffer. Using our measured ER volume, we calculated the molarity of calreticulin in the ER and considered that calreticulin can bind up to 25 calcium ions[37] (Supplementary Table 7). Calreticulin is supposed to bind around 50% of all calcium in the ER[38]. Since the concentration in the ER has been determined to be around 200 µM[39], it would be able to do so in stubby spines but not in mushroom spines. There are several explanations for this. First, there might be other proteins present in mushroom spines, especially in the spine apparatus, that also buffer calcium. Second, the calcium concentration in the spine apparatus might be lower than in traditional ER, therefore requiring less calreticulin. Third, and most likely, it is possible that we attributed less calreticulin to mushroom spines than actually present there because most of the ER is present in the shaft and therefore might be partially excluded by focusing on the mushroom spine alone, but not when analyzing the stubby spines.

Finally, we turned to the question of whether our measured spine proteome could be sustained by local translation, a long-standing hypothesis in the field[40]. To do so, we calculated the amount of protein sequences that need to be produced every day. Each protein population needs to be replaced in accordance with its own half-life, and each individual protein will take a different amount of time to be produced, depending on the protein length. Protein sequence lengths were obtained from UniProt, while half-life values were obtained from previous measurements in neuron-enriched hippocampal cultures reported by Dörrbaum and colleagues[41]. For proteins that were not measured in this article, we set the half-life to the mean half-life of all other dendritic spine proteins in our dataset ($\tau = 5.302$ days). Taking into account these parameters, we estimated that a total number of 16,695,693 amino acids need to be incorporated into proteins in a dendritic spine within 24 h.

We then determined how many amino acids could be incorporated into proteins in dendritic spines by using our measured ribosomal proteins as a proxy for the copy number of available ribosomes. We considered the lowest number we measured to render this into a conservative approach (Rpl7a = 241). Using a ribosome speed of 157.8 amino acids per min (ref. [42]) and a fraction of active ribosomes of 0.7 (refs. [43,44]), we calculated that 230% of our measured spine proteome could be locally synthesized. As we know that our measured proteome only covers 47% of the total spine proteome (Fig. 4), we arrived at a final percentage of 108% that could be locally maintained. Therefore, under our assumptions, the complete spine proteome could be locally produced, which is in line with several reports that have shown this for individual spine proteins, such as CaMKII[45].

Discussion

Our study, based on a combination of fluorescence imaging, EM and biochemical investigations, produced a large database of measurements on cultured spines. This resource covers information ranging from protein copy numbers to morphological parameters of spines and protein localization data. In principle, our measurements can now be employed in studying how the various spine parameters might affect cellular processes, such as trafficking, translation and calcium dynamics, as indicated above.

However, several limitations should still be taken into account. First, to overcome the limitations imposed by the use of cultures, we suggest that comparative studies be performed between the current dataset, obtained in culture, and in vivo samples. We established a comparative imaging approach[46] to enable this type of analysis, which should help rapidly place copy numbers in a variety of synapses[47].

Second, we only studied here two major types of spines, since other ones were far less abundant in our preparations. Future studies should help decipher the quantitative proteomes of different, additional types of spines.

Taking these limitations into account, our work should help with testing several important hypotheses, including the idea that the similarity between stubby and mushroom spines is due to individual spines switching shapes over time between the two types or that glial cells are important in determining further differences between stubby and mushroom spines (for example, through the interaction of astrocytic feet and synapses).

Online content

Any methods, additional references, Nature Research reporting summaries, source data, extended data, supplementary information, acknowledgements, peer review information; details of author contributions and competing interests; and statements of data and code availability are available at https://doi.org/10.1038/s41593-021-00874-w.

Received: 26 September 2020; Accepted: 13 May 2021;
Published online: 24 June 2021

References

1. Humeau, Y. & Choquet, D. The next generation of approaches to investigate the link between synaptic plasticity and learning. *Nat. Neurosci.* **22**, 1536–1543 (2019).
2. Bourne, J. N. & Harris, K. M. Balancing structure and function at hippocampal dendritic spines. *Annu. Rev. Neurosci.* **31**, 47–67 (2008).
3. Forrest, M. P., Parnell, E. & Penzes, P. Dendritic structural plasticity and neuropsychiatric disease. *Nat. Rev. Neurosci.* **19**, 215–234 (2018).
4. Berry, K. P. & Nedivi, E. Spine dynamics: are they all the same? *Neuron* **96**, 43–55 (2017).
5. Harris, K. M., Jensen, F. E. & Tsao, B. Three-dimensional structure of dendritic spines and synapses in rat hippocampus (CA1) at postnatal day 15 and adult ages: implications for the maturation of synaptic physiology and long-term potentiation. *J. Neurosci.* **12**, 2685–2705 (1992).
6. Spacek, J. & Harris, K. M. Three-dimensional organization of smooth endoplasmic reticulum in hippocampal CA1 dendrites and dendritic spines of the immature and mature rat. *J. Neurosci.* **17**, 190–203 (1997).
7. Tønnesen, J., Katona, G., Rózsa, B. & Nägerl, U. V. Spine neck plasticity regulates compartmentalization of synapses. *Nat. Neurosci.* **17**, 678–685 (2014).
8. Araya, R. Input transformation by dendritic spines of pyramidal neurons. *Front. Neuroanat.* https://doi.org/10.3389/fnana.2014.00141 (2014).
9. Nakahata, Y. & Yasuda, R. Plasticity of spine structure: local signaling, translation and cytoskeletal reorganization. *Front. Synaptic Neurosci.* **10**, 29 (2018).
10. Biederer, T., Kaeser, P. S. & Blanpied, T. A. Transcellular nanoalignment of synaptic function. *Neuron* **96**, 680–696 (2017).
11. Patriarchi, T., Buonarati, O. R. & Hell, J. W. Postsynaptic localization and regulation of AMPA receptors and Cav1.2 by β2 adrenergic receptor/PKA and Ca^{2+}/CaMKII signaling. *EMBO J.* **37**, e99771 (2018).
12. Papa, M., Bundman, M. C., Greenberger, V. & Segal, M. Morphological analysis of dendritic spine development in primary cultures of hippocampal neurons. *J. Neurosci.* **15**, 1–11 (1995).
13. Kaech, S. & Banker, G. Culturing hippocampal neurons. *Nat. Protoc.* **1**, 2406–2415 (2006).
14. Richter, K. N. et al. Glyoxal as an alternative fixative to formaldehyde in immunostaining and super-resolution microscopy. *EMBO J.* https://doi.org/10.15252/embj.201695709 (2017).
15. Hruska, M., Henderson, N., Le Marchand, S. J., Jafri, H. & Dalva, M. B. Synaptic nanomodules underlie the organization and plasticity of spine synapses. *Nat. Neurosci.* https://doi.org/10.1038/s41593-018-0138-9 (2018).
16. Ikeda, K. & Bekkers, J. M. Counting the number of releasable synaptic vesicles in a presynaptic terminal. *Proc. Natl Acad. Sci. USA* **106**, 2945–2950 (2009).

17. Schanzenbächer, C. T., Sambandan, S., Langer, J. D. & Schuman, E. M. Nascent proteome remodeling following homeostatic scaling at hippocampal synapses. *Neuron* **92**, 358–371 (2016).
18. Schanzenbächer, C. T., Langer, J. D. & Schuman, E. M. Time- and polarity-dependent proteomic changes associated with homeostatic scaling at central synapses. *eLife* **7**, e33322 (2018).
19. Ziv, N. E. & Brenner, N. Synaptic tenacity or lack thereof: spontaneous remodeling of synapses. *Trends Neurosci.* **41**, 89–99 (2018).
20. Urban, N. T., Willig, K. I., Hell, S. W. & Nägerl, U. V. STED nanoscopy of actin dynamics in synapses deep inside living brain slices. *Biophys. J.* **101**, 1277–1284 (2011).
21. Nägerl, U. V., Willig, K. I., Hein, B., Hell, S. W. & Bonhoeffer, T. Live-cell imaging of dendritic spines by STED microscopy. *Proc. Natl Acad. Sci. USA* **105**, 18982–18987 (2008).
22. Willig, K. I. et al. Nanoscopy of filamentous actin in cortical dendrites of a living mouse. *Biophys. J.* **106**, L01–L03 (2014).
23. Wegner, W. et al. In vivo mouse and live cell STED microscopy of neuronal actin plasticity using far-red emitting fluorescent proteins. *Sci. Rep.* **7**, 11781 (2017).
24. Wegner, W., Mott, A. C., Grant, S. G. N., Steffens, H. & Willig, K. I. In vivo STED microscopy visualizes PSD95 sub-structures and morphological changes over several hours in the mouse visual cortex. *Sci. Rep.* **8**, 219 (2018).
25. Turrigiano, G. G., Leslie, K. R., Desai, N. S., Rutherford, L. C. & Nelson, S. B. Activity-dependent scaling of quantal amplitude in neocortical neurons. *Nature* **391**, 892–896 (1998).
26. Gallimore, A. R., Kim, T., Tanaka-Yamamoto, K. & De Schutter, E. Switching on depression and potentiation in the cerebellum. *Cell Rep.* **22**, 722–733 (2018).
27. Freer, R. et al. Supersaturated proteins are enriched at synapses and underlie cell and tissue vulnerability in Alzheimer's disease. *Heliyon* https://doi.org/10.1016/j.heliyon.2019.e02589 (2019).
28. Wilhelm, B. G. et al. Composition of isolated synaptic boutons reveals the amounts of vesicle trafficking proteins. *Science* **344**, 1023–1028 (2014).
29. Kirchhausen, T., Owen, D. & Harrison, S. C. Molecular structure, function, and dynamics of clathrin-mediated membrane traffic. *Cold Spring Harb. Perspect. Biol.* **6**, a016725 (2014).
30. McMahon, H. T. & Boucrot, E. Molecular mechanism and physiological functions of clathrin-mediated endocytosis. *Nat. Rev. Mol. Cell Biol.* **12**, 517–533 (2011).
31. Pearse, B. M. & Crowther, R. A. Structure and assembly of coated vesicles. *Annu. Rev. Biophys. Biophys. Chem.* **16**, 49–68 (1987).
32. Blanpied, T. A., Scott, D. B. & Ehlers, M. D. Dynamics and regulation of clathrin coats at specialized endocytic zones of dendrites and spines. *Neuron* **36**, 435–449 (2002).
33. Esteves da Silva, M. et al. Positioning of AMPA receptor-containing endosomes regulates synapse architecture. *Cell Rep.* **13**, 933–943 (2015).
34. Shnyrova, A. V. et al. Geometric catalysis of membrane fission driven by flexible dynamin rings. *Science* **339**, 1433–1436 (2013).
35. Zheng, K. et al. Time-resolved imaging reveals heterogeneous landscapes of nanomolar Ca^{2+} in neurons and astroglia. *Neuron* **88**, 277–288 (2015).
36. Higley, M. J. & Sabatini, B. L. Calcium signaling in dendritic spines. *Cold Spring Harb. Perspect. Biol.* **4**, a005686 (2012).
37. Park, B. J. et al. Calreticulin, a calcium-binding molecular chaperone, is required for stress response and fertility in *Caenorhabditis elegans*. *Mol. Biol. Cell* **12**, 2835–2845 (2001).
38. Nakamura, K. et al. Functional specialization of calreticulin domains. *J. Cell Biol.* **154**, 961–972 (2001).
39. Solovyova, N., Veselovsky, N., Toescu, E. C. & Verkhratsky, A. Ca^{2+} dynamics in the lumen of the endoplasmic reticulum in sensory neurons: direct visualization of Ca^{2+}-induced Ca^{2+} release triggered by physiological Ca^{2+} entry. *EMBO J.* **21**, 622–630 (2002).
40. Biever, A., Donlin-Asp, P. G. & Schuman, E. M. Local translation in neuronal processes. *Curr. Opin. Neurobiol.* **57**, 141–148 (2019).
41. Dörrbaum, A. R., Kochen, L., Langer, J. D. & Schuman, E. M. Local and global influences on protein turnover in neurons and glia. *eLife* **7**, e34202 (2018).
42. Riba, A. et al. Protein synthesis rates and ribosome occupancies reveal determinants of translation elongation rates. *Proc. Natl Acad. Sci. USA* **116**, 15023–15032 (2019).
43. Alberghina, F. A. M., Sturani, E. & Gohlke, J. R. Levels and rates of synthesis of ribosomal ribonucleic acid, transfer ribonucleic acid, and protein in *Neurospora crassa* in different steady states of growth. *J. Biol. Chem.* **250**, 4381–4388 (1975).
44. Forchhammer, J. & Lindahl, L. Growth rate of polypeptide chains as a function of the cell growth rate in a mutant of *Escherichia coli* 15. *J. Mol. Biol.* **55**, 563–568 (1971).
45. Miller, S. et al. Disruption of dendritic translation of CaMKIIα impairs stabilization of synaptic plasticity and memory consolidation. *Neuron* **36**, 507–519 (2002).
46. Richter, K. N. et al. Comparative synaptosome imaging: a semi-quantitative method to obtain copy numbers for synaptic and neuronal proteins. *Sci. Rep.* **8**, 14838 (2018).
47. Zhu, F. et al. Architecture of the mouse brain synaptome. *Neuron* **99**, 781–799.e10 (2018).
48. Ciryam, P., Tartaglia, G. G., Morimoto, R. I., Dobson, C. M. & Vendruscolo, M. Widespread aggregation and neurodegenerative diseases are associated with supersaturated proteins. *Cell Rep.* **5**, 781–790 (2013).
49. Fornasiero, E. F. et al. Precisely measured protein lifetimes in the mouse brain reveal differences across tissues and subcellular fractions. *Nat. Commun.* **9**, 4230 (2018).
50. Mandad, S. et al. The codon sequences predict protein lifetimes and other parameters of the protein life cycle in the mouse brain. *Sci. Rep.* **8**, 16913 (2018).

Methods

Antibodies and chemicals. The antibodies and chemicals used in this study are detailed in Supplementary Table 1.

Neuronal cultures. We prepared hippocampal cultured neurons from E18 Wistar rats placed in a sandwich configuration[13] relying on N2-supplemented medium. We changed the protocol as follows: we first seeded glia at 10,000 cells per well in 12-well plates 3 days before the dissection of the E18 rats. We then seeded the neurons at 30,000 cells per 18-mm coverslip, using paraffin dots as a spacer between the neurons and the glia. Twice a week, we exchanged 500 µl of the cell culture medium with fresh medium. As paraffin interferes with MS analyses, we replaced them with C-shaped rings, cut from 1-mm-thick Teflon sheets (Alt Industriebedarf), with 20-mm outer and 14-mm inner diameters. These spacers were thoroughly washed with ethanol (70%) and were autoclaved before use.

Homeostatic plasticity. We treated the cultures with 20 µM bicuculline (Sigma) or with 1 µM TTX (Tocris) for 72 h. The former treatment induces synaptic downscaling, while the latter induces upscaling[51].

Membrane-attached GFP transfections. The construct for the membrane-bound form of EGFP, which consists of a palmitoylation sequence of GAP43 linked to the amino terminus of GFP, was purchased from Addgene (plasmid 14757). This was transfected by magnetofection using the manufacturer's protocol (OZ Biosciences). The plasmid has been previously characterized[52].

EM. Cells were embedded in Epon, following previously published protocols[53], cut into multiple consecutive sections and were imaged with a Zeiss electron microscope (EM902; Zeiss), using a 1,024×1,024 CCD detector (type Proscan CCD HSS 512/1024; Proscan Electronics). The synapses were then detected by monitoring the existence of an evident PSD, as well as evident presynapses, loaded with synaptic vesicles docked to a clear presynaptic active zone. The respective image areas were then aligned using Photoshop (Adobe Systems). The outlines of the membrane (starting from the first protrusion from the otherwise relatively level shaft membrane), PSD, mitochondria and vacuoles were traced in each section. The positions of small vesicles (of synaptic vesicle size and shape) were also measured. This enabled the generation of 3D reconstructions, as well as measurements of volumes and surfaces. To estimate the total protein amount in dendritic spines, ideally, we would isolate and purify them, followed by protein amount estimates by biochemical means. As this is not possible, we compared the EM density in spines to the total intensity in presynapses, where the protein concentration is known from[28]. This type of analysis has been used in the past to compare protein amounts in different locations[28,54].

Immunostainings. At days in vitro 21–23, neurons were fixed using either paraformaldehyde or a glyoxal solution at pH 4 (ref. [14]). The cultures were then quenched using 100 mM NH_4Cl, in PBS (30 min), were permeabilized with 0.3% Tween (in PBS containing 2.5% BSA (ribosomal protein stainings were performed with 5% BSA) three times for 5 min each time). Primary antibodies were then added to the cultures, in the same buffer, and were incubated for 60 min in a humidified chamber. The cultures were washed with the same buffer for at least 15 min, with several buffer exchanges. Secondary antibodies were then added and incubated as described above. The cultures were washed with high-salt PBS (with 500 mM NaCl, three times, 5 min each) and then with normal PBS (twice, 5 min each). Meanwhile, DiO crystals were placed in PBS (20 µg ml^{-1}) and were sonicated, using a water-bath sonicator, for 30 min. A further tenfold dilution of DiO followed, and 1 ml of DiO solution was incubated in each well after the last PBS wash for 20 min at 37 °C. After a brief wash in PBS, the cells were incubated in PBS overnight, were washed again with PBS (twice, 5 min each) and were embedded in self-made Mowiol.

Fluorescence microscopy. We relied on DiO to identify the plasma membrane, while Homer1 was used as a PSD marker (immunostained with unconjugated primary antibodies and Cy3-conjugated secondary antibodies). The protein of interest was detected with unconjugated primary antibodies and Atto647N-conjugated secondary antibodies. Epifluorescence imaging was performed using a Nikon Eclipse Ti-E microscope (Nikon Instruments), equipped with a ×100 1.4 NA UPlanSApo oil-immersion objective and a DS-Qi 2 CMOS camera (Nikon Instruments). STED and confocal imaging were performed using a Leica TCS STED microscope (Leica Microsystems) equipped with a ×100 1.4 NA ×100 HCX PL APO CS oil-immersion objective (Leica Microsystems). DiO was excited using an argon laser 488-nm line, while Cy3 was excited using a helium-neon laser (543 nm) or a DPSS laser (561 nm). Acusto-optic tunable filters were used to obtain suitable emission wavelengths. Atto647N was excited using a 635-nm diode laser. STED was induced using a 750-nm depletion beam from a Spectra-Physics MaiTai multiphoton laser (Newport Spectra-Physics). Detection was performed using photomultiplier tubes or by hybrid detectors for confocal mode, or with an avalanche photodiode (Leica Microsystems) for STED mode. Pixels sizes were kept at 20.21 nm. We analyzed at least two independent neuronal cultures for each protein of interest, and at least ten images were collected for each experiment. Between 72 and 276 images were analyzed for mushroom spines (average of 175 spines per protein). Between 44 and 248 images were analyzed for stubby spines (average of 134 spines per protein). See Supplementary Table 5 for detailed information.

Image analysis. All analysis was performed using Matlab 2017b (MathWorks). To determine the average distributions of spine proteins, we first aligned the STED images of the spines to the DiO and Homer1 images (relying on a confocal image of the protein of interest, which was taken in parallel, line by line, with the DiO and Homer1 images). Each spine was then selected, relying on the DiO mask and on the Homer1 mask. A smaller selection (6×6-µm sized subimage) was then saved for further processing, centered on the respective synapse. The synapses were then assigned an identity (mushroom, stubby or other (neither stubby nor mushroom)) by an expert in the laboratory. Then, a manual identification of spine landmarks followed: the top, bottom, left and right edges of the spine head, as well as the top and bottom positions of the neck and shaft junctions. A rectangular region on the dendritic shaft, in the immediate vicinity of the spine, was then marked to enable calculation of the protein enrichment in the spine in comparison to the dendritic shaft. An accurate tracing of the neck position was also manually performed for the mushroom spines. We then aligned all the spines using these landmarks. The DiO mask was used to remove all fluorescence coming from outside the spine before any further processing. To avoid any problems with different average signal intensities between replicates, the intensity levels of all spines in one preparation were normalized to the maximal intensity observed in the respective preparation. A filtering procedure, based on a median filter (2×2 pixels), was then followed by background subtraction, before averaging all spine images, to obtain representative overall images as shown in Fig. 1a.

For the analysis of the zone enrichment, we separated the space of the dendrites into different zones, as described in Fig. 1 and Extended Data Fig. 5. We then calculated the fraction of the signal present in each zone (normalized by zone area) for each individual protein as well as for an average of all proteins (marked as "total protein" in the figures). For each protein, we then described the fold difference for each zone between the signal present in every bin and the signal from the respective bins for the "total protein" distribution.

To analyze different characteristics of individual spines, we used the landmarks manually applied onto spines as described above to automatically extract different morphological parameters, including the positions of the head, shaft and neck, and their areas. The PSD (Homer1) signal was automatically processed to provide the PSD size (from the full width at half maximum (FWHM) of the respective signal), its area, eccentricity and position. We also analyzed the individual STED spots, whose characteristics are reported in Supplementary Data 1. They were detected by employing a wavelet transformation, using a Spot Detector plugin for icy[55,56]. The scale 2 was used, and an 80% threshold. For clarity, outliers exceeding the range of median ± 5 standard deviations are not shown.

The following measurements were performed:

1. Head enrichment (average signal in the head region divided by average signal in the marked shaft region that was previously marked, as indicated above).
2. PSD enrichment (same as above, but with the signal measured in the Homer1 area, centered on the center of mass of the Homer1 signal, and with the width set by the FWHM of the Homer1 spot).
3. Nearest neighbor (the distance of each spot to the nearest spot).
4. The distance to the PSD (from every STED spot in the head of a mushroom spine, or in the synaptic region of a stubby spine, to the PSD).
5. Eccentricity (the position of spots in the head, in relation to the top–bottom direction; this value approaches 1 for spots found exclusively at the top of the head region and −1 for spots at the bottom of the head region).
6. Laterality (similar to eccentricity, but in the horizontal direction. However, as we expect spines to have a rotational symmetry, the left and right dimensions are considered to be equal. Signals do not vary from 1 to −1, but rather from 1 to 0, where 0 is in the head center and 1 is on the extreme left or right).

For the analysis of the protein correlation to the synaptic strength (Fig. 5), we relied on the correlation of the Homer1 intensity to the intensity of the signal of the protein of interest across all spines of one specific class (stubby or mushroom).

Representative images shown in Supplementary Data 1 were mildly deconvolved, using Huygens Essential 18.10, to improve clarity.

For the analysis of nanomodules, the STED signal was smoothed using a Gaussian filter, and the intensity was normalized to follow a standard-normal distribution. Only the head region was considered, which was determined by fitting an ellipse to the annotated head coordinates. To detect nanomodules, we used the adaptive thresholding technique in Matlab and filtered out spots below 80-nm radius, as previously reported[15].

Gauss shift clustering. Clustering methods assign data objects to groups called clusters. Objects within a cluster are similar to each other while objects from different clusters are dissimilar. Density attractor clustering (DAC) first builds a model that describes how probable it is that a certain new object appears in a certain region. The model is built using the statistical method kernel density estimation, which calculates the probability density function (PDF) for the respective dataset. DAC considers all objects located on the same "hill" of the PDF to belong to the

same cluster and "hill tops" (local maxima of the PDF, named "modes") to be cluster centers. This approach was originally presented by Wishart[57]. DAC has two major advantages over parametric clustering methods like *k*-means that are important for our case. First, DAC does not require the number of clusters a priori, and second, we are able to validate whether a specific segmentation is valid. Here, we do not know how many clusters exist. Using *k*-means, one might try to cluster the dataset multiple times providing different numbers of expected clusters. Then, for the measure of the quality, the best clustering result with the optimal number of clusters can be chosen. However, while this approach might provide the 'best' clustering result, it does not provide information on whether the result is 'good enough' or whether there simply a valid clustering does not exist.

Here, DAC provides a solution. For DAC, one has to provide a model parameter called the bandwidth (also known as the "scale"), which describes how coarse or finely granulated the segmentation is supposed to be. By varying the bandwidth from small (finely granulated) to large (coarse), we receive for each bandwidth value the corresponding number of resulting clusters. If the number of clusters is stable across a relatively large range of bandwidth values, we can conclude that the segmentation is valid and that the corresponding number of clusters is the "true" number of clusters. This reasoning is substantiated by scale-space theory and scale-space filtering in general[58] and respective clustering in particular[59]. For finding the modes of the PDF, we use Gauss shift[60], which is similar in results to mean shift[61], but much more efficient.

To find out whether mushroom and stubby spines are similar, we argue that the two types should be naturally separable: we expect two distinct local maxima of the PDF over the space of different spine shapes to form. For our experiment, we disregard the features NeckArea and NeckLength for the mushroom-shaped spines, and considered the features HeadArea, HeadHeight, HeadWidth, HomerArea, HomerMajorAxisLength, HomerMinorAxisLength and HomerMeanIntensity. As it turns out, there is no such valid segmentation that would allow us to separate mushroom and stubby spines. Thus, we have to conclude that, at least for the used features, there is no significant difference between them.

This conclusion was reached by clustering the seven-dimensional dataset for different bandwidths and determining the number of resulting clusters. To have reference curves, we created two seven-dimensional artificial datasets: for one, we drew from a single multivariate Gaussian distribution (a dataset that cannot be segmented in a valid way), for the other, we drew from three distinctly separated Gaussian distributions (a dataset that can be segmented into three clusters in a valid way). As we can see in Extended Data Fig. 3, the resulting scale-space graph for the spine dataset is much closer in shape to the non-clusterable dataset than the clusterable dataset. To visualize the PDF of the dataset, we linearly transformed the dataset using principal component analysis. The two most important dimensions of the transformed dataset (principal components) are displayed in Extended Data Fig. 3, with the corresponding density: while the density is not smooth, the overall trend is undoubtedly that there is only one cluster.

MS. Protein concentrations in all samples were first estimated using BCA protocols[62]. We then added 10 µl of RapiGest (1%, Waters) for 20 µg protein (either neuronal cultures or UPS2 standard proteins) and we incubated the samples at 95 °C (5 min). Further steps were then performed under rotation using a Thermomixer (300 r.p.m.) at room temperature, and started with the addition of 10 µl of ammonium bicarbonate (100 mM, for 5 min) followed by the addition of 10 µl of dithiothreitol (dissolved in 100 mM ammonium bicarbonate, and added for 60 min). Afterwards 10 µl iodoacetamide (100 mM, dissolved in 100 mM ammonium bicarbonate) was added, followed by incubation for 20 min (protected from light). The samples were then diluted by the addition of 180 ml of ammonium bicarbonate solution (100 mM), to reduce the percentage of detergent below 0.1%, and trypsin (ProMega, diluted 1 to 50) was added for protein digestion.

When long gradients were desired, samples were digested for 12–18 h. For high pH fractionation, the samples (30 µg) were digested for only 16 h. This process was terminated by the addition of 5% formic acid (20 ml). This was followed by an incubation period with 20 µl of 5% trifluoroacetic acid (120 min), to destroy the RapiGest molecules, and by desalting using Stage Tips. We fitted at least four C_{18} plugs in one micropipette tip, thereby generating one column, which was washed with methanol (twice, each time with 50 µl methanol), and was equilibrated with 0.1% formic acid (twice). The solution containing the peptides was loaded onto the columns, and the peptides were allowed to bind the column before washing with formic acid (0.1%, 4 times) to remove ions. The peptides were then eluted using acetonitrile (80%, with 0.1% formic acid), and the eluate was dried using a SpeedVac concentrator.

We then used an Orbitrap Fusion Lumos Tribrid mass spectrometer (Thermo Fisher Scientific) to process the samples, using a long gradient of 4 h. Alternatively, they were fractionated by high pH and were processed using a Q-Exactive HF mass spectrometer (Thermo Fisher Scientific) for liquid chromatography–MS for a short gradient (1 h).

For the regular iBAQ with long gradients, the resuspended samples in loading buffer were analyzed using an online UltiMate 3000 RSLCnano HPLC system (Thermo Fisher Scientific), coupled online to an Orbitrap Fusion Lumos Tribrid mass spectrometer (Thermo Fisher Scientific). Peptides were desalted for 3 min using a reverse-phase C_{18} pre-column (length of 3 cm, inner diameter of 100 µm, outer diameter of 360 mm). They were then switched to an analytical column (length of 30 cm, inner diameter of 75 µm), generated with ReproSil-Pur C_{18} AQ 1.9-µm reversed-phase resin (Dr. Maisch). A linear gradient of 5–30% buffer B was used to separate peptides, at 10 nl min^{-1}. We used a long gradient of 238 min on the Lumos, with all steps performed at 50 °C.

We set the scan range of precursors from 350 to 1,500 *m/z*, at a resolution of 120,000 in Top Speed mode. Top intense precursors were fragmented in the HCD cell and were analyzed at a resolution 30,000. The AGC target and the isolation window were set at 5×10^4 and with an isolation window of 1.6 *m/z*.

For high pH fractionation, we injected 40 µg of digested proteins on a reversed-phase column (XBridge Waters C18 column of dimension 3.5 µm, 1.0 × 150 mm) installed on an Agilent 1200 HPLC system for 1 h. We used the dual highly basic buffer system (buffer A: 100% 10 mM ammonia; buffer B: 90% acetonitrile containing 10 mM ammonia) to create a linear gradient. Peptides were loaded on the column in buffer A (5 min). This was followed by the application of a gradient of buffer B, 0–50%, for 45 min. The column was then washed using 95% buffer B (5 min) and was returned to buffer A (100%) for 5 min, using a flow rate of 50 µl min^{-1}. We collected 60 fractions, and we pooled them to 12 final fractions in a staggered manner. These were dried as above, using a SpeedVac, and were resuspended in 25 µl of loading buffer (5% acetonitrile and 0.1% trifluoroacetic acid), and were injected into a Q-Exactive HF mass spectrometer (Thermo Fisher Scientific), using, or a short gradient of 58 min.

Here, the precursors were scanned in a mass range from 350 to 1,600 Da at a resolution of 60,000 at 200 *m/z*. The top 30 precursor ion were chosen for MS1 by using data-dependent acquisition (DDA) mode at a resolution of 15,000 at 200 *m/z*, with maximum IT of 50 ms. For MS2, HCD fragmentation was performed with the AGC target fill value of 1×10^5 ions. The precursors were isolated with a window of 1.4 Da. The lock mass option (445.1200 *m/z*) was used for internal recalibration.

For each sample, we analyzed 1 µg of UPS2 standard proteins before and after the run, which enabled us to use iBAQ to estimate protein amounts in the samples in a label-free fashion. Protein identifications were performed using MaxQuant software (Cox and Mann, 2008), v.1.5.3.8 or 1.6.0.16, using the Andromeda search engine, relying on rat SwissProt (December 2016; containing 29,795 entries) and the Human Universal Proteome Standard (UPS2, Sigma-Aldrich) database. Tolerances of 6 ppm (for MS) and 10 ppm (for MS/MS) were set during the database searches. We set the oxidation of methionine and carbamidomethylation of cysteines as variable and fixed modifications, respectively. Tryptic specificity with no proline restriction, and up to two missed cleavages, was used. The false discovery rate was set to 1%. The iBAQ option was enabled for quantification (using the $\log_{10}$ fit).

The biological replicates were digested for 8, 12, 16, 24 and 48 h, and the maximum iBAQ value (from the long and the short gradient) was selected to provide the abundances of the different proteins, relying on the UPS2 protein analysis[63]. We then median-normalized the data, and we calculated, for each protein, the average across all biological replicates. To transform the protein copy numbers in the sample (per µg total protein) into copy numbers per neuron, we counted the neuron nuclei in Hoechst stainings on sister coverslips from the preparations used for MS, which enabled the calculation of neuronal numbers per µg protein, and thereby enabled the calculation of protein copy numbers per neuron.

Determination of the protein copy numbers per spine. For each protein of interest, we imaged large fields of view in epifluorescence, using Homer1 as a postsynaptic marker, using at least two independent cultures and at least 20 images per replicate. This enabled us to then calculate the percentage of the signal that was found within the Homer1-marked synapses. To account for the low resolution of this procedure, which cannot determine whether the respective signals are specific to the postsynapse or may also be derived from presynapses situated close to the Homer1 signals, we then calculated the correlation coefficient *R* of the respective proteins of interest to the Homer1 signals obtained in STED imaging (normalized to the maximum expected *R* for Homer1 double-immunostainings). The percentage in the Homer1-marked synapses was then corrected by multiplying with the *R* value. This procedure served to increase the accuracy of our calculations and successfully removed contamination from presynaptic proteins, such as synaptophysin. This analysis provided the overall fraction of the signal that was present in all spines of a neuron. Knowing the copy number of a given protein (see the previous section) in the neuron and the number of spines per neuron (~300) enabled us to calculate the copy numbers per spine as follows:

$$\text{Copy number}_{\text{spine}} = \frac{\text{copy number}_{\text{neuron}} \times \text{percentage in Homer1 mask} \times \frac{R_{\text{protein of interest}}}{R_{\text{Homer1}}}}{\text{spines per neuron}}$$

MS comparison of brain lysate to Banker culture. Rat brain homogenate was prepared and run in iBAQ mode as described above and run in eight technical replicates. Cell-type-specific proteins were selected and compared between brain homogenate and the results from the Banker cells from above.

Immunoblotting. Immunoblotting was done essentially as previously described[64]. The purified proteins that were used as standards are detailed in Supplementary Table 1.

Comparison of the neuron proteome with mushroom, stubby and presynaptic proteome. To estimate the protein molarity, the concentration and the volume in the total neuron, we assumed a neuron volume of 5×10^3 µm based on values derived from mammalian cell cultures[65–70] and calculated the total protein copies across our MS dataset. Because the PDB does not contain 3D structures for most of the proteins (>6,000 different proteins), we also assumed an average protein volume of 3.35×10^{-8} µm (based on ref. [71]). To calculate the same measurements for mushroom and stubby spines, we used only the dendritic spine proteome (110 proteins). For these proteins, we used their individual 3D volumina, as retrieved from the PDB. The data on the presynapse was extracted from ref. [28].

Comparative synaptosome imaging. Extremely long proteins (>175 kDa), or proteins with more than four transmembrane domains, are difficult to quantify in iBAQ MS. To alleviate this problem, we additionally performed CoSi-Quant[46] for these proteins and averaged the results obtained with iBAQ and CoSi-Quant.

Calculation of feature maps. Analysis was done using Python 3.7 and Matlab 2019b. We extracted feature scores from published sources[48–50]. We then calculated the total score of each voxel in our model by multiplying each protein score with the copy number of the respective protein in the voxel and summed over all proteins (except for mitochondrial proteins, as the stubby model does not contain a mitochondrion). To obtain the average score per voxel, we normalized the feature map by dividing each voxel score by the total protein copy number contained in it. For the presynapse, we used the protein locations from ref. [23] and binned them using $25 \times 25 \times 100$-nm sized voxels.

Statistics and reproducibility. All data are shown as the mean ± s.e.m. unless stated otherwise. Violin plots show the median and quartiles. We performed all statistics using Matlab 2017b or GraphPad Prism 8 (GraphPad). Data were tested for normal distribution using the D'Agostino–Pearson test. When data were normally distributed, we used two-tailed *t*-tests for single comparisons or one-way analysis of variance (ANOVA) with Bonferroni correction for multiple comparisons unless stated otherwise. In cases of the data not following a normal distribution, we used the Mann–Whitney (rank-sum) test for single comparisons or the Kruskal–Wallis test with Dunn's correction for multiple comparisons unless stated otherwise. The maximum number of experiments were performed and no statistical methods were used to predetermine sample sizes. No data were excluded from analyses. With the exception of the plasticity experiments, this study did not compare different conditions, therefore experiments were not randomized and investigators were not blinded to allocation during experiments and outcome assessment.

3D model generation. Protein localization was projected into the 3D space of two spines that most closely represented the average mushroom and stubby spines, reconstructing the membrane computationally[72] and using the zone definitions presented in Extended Data Fig. 5. As the zones in 3D occasionally contained regions of both membrane and cytosol, or different organelles, the final distribution of the proteins was manually performed. Membrane proteins were assigned to the correct membrane areas, and organelle identities (as defined in Extended Data Fig. 5) were respected, taking into account the known organelle distributions of the different spine proteins derived from the literature (Supplementary Table 4). Protein shapes and sizes were extracted from PDB or generated with I-Tasser[73,74], rendered using Autodesk Maya (Autodesk) following previously presented procedures[23].

Animals. Wild-type Wistar rats (*Rattus norvegicus*) for the preparation of primary hippocampal neuron cultures and synaptosomes were obtained from the University Medical Center Göttingen. All animals were handled according to the specifications of the University of Göttingen and of the local authority, the State of Lower Saxony (Landesamt für Verbraucherschutz, LAVES, Braunschweig, Germany). All animal experiments were approved by the local authority, the Lower Saxony State Office for Consumer Protection and Food Safety (Niedersächsisches Landesamt für Verbraucherschutz und Lebensmittelsicherheit).

Reporting Summary. Further information on research design is available in the Nature Research Reporting Summary linked to this article.

Data availability

The MS proteomics data have been deposited to the ProteomeXchange Consortium via the PRIDE partner repository with the dataset identifier PXD015308. Image data are available from the corresponding author upon reasonable request.

Code availability

Code is available on GitHub: https://github.com/MSHelm/Nanomap.

References

51. Turrigiano, G. G. The self-tuning neuron: synaptic scaling of excitatory synapses. *Cell* **135**, 422–435 (2008).
52. Matsuda, T. & Cepko, C. L. Controlled expression of transgenes introduced by in vivo electroporation. *Proc. Natl Acad. Sci. USA* **104**, 1027–1032 (2007).
53. Schikorski, T. & Stevens, C. F. Quantitative ultrastructural analysis of hippocampal excitatory synapses. *J. Neurosci.* **17**, 5858–5867 (1997).
54. Collins, M. O. et al. Molecular characterization and comparison of the components and multiprotein complexes in the postsynaptic proteome. *J. Neurochem.* **97**, 16–23 (2006).
55. De Chaumont, F. et al. Icy: an open bioimage informatics platform for extended reproducible research. *Nat. Methods* **9**, 690–696 (2012).
56. Olivo-Marin, J. C. Extraction of spots in biological images using multiscale products. *Pattern Recognit.* **35**, 1989–1996 (2002).
57. Wishart, D. M. G. in *Numerical Taxonomy* (ed. Cole, A. J.) 282–311 (Academic Press, 1969).
58. Witkin, A. Scale-space filtering: a new approach to multi-scale description. In *Proc. ICASSP '84. IEEE International Conference on Acoustics, Speech, and Signal Processing* 9 150–153 (Institute of Electrical and Electronics Engineers, 1983).
59. Leung, Yee, Zhang, Jiang-She & Xu, Zong-Ben Clustering by scale-space filtering. *IEEE Trans. Pattern Anal. Mach. Intell.* **22**, 1396–1410 (2000).
60. Leibrandt, R. & Günnemann, S. Gauss Shift: Density Attractor Clustering Faster than Mean Shift. In *Proc. ECML-PKDD 2020*: *The European Conference on Machine Learning and Principles and Practice of Knowledge Discovery in Databases (ECML-PKDD)* 14–18 (2020).
61. Fukunaga, K. & Hostetler, L. The estimation of the gradient of a density function, with applications in pattern recognition. *IEEE Trans. Inf. Theory* **21**, 32–40 (1975).
62. Smith, P. K. et al. Measurement of protein using bicinchoninic acid. *Anal. Biochem.* **150**, 76–85 (1985).
63. Schwanhäusser, B. et al. Global quantification of mammalian gene expression control. *Nature* **473**, 337–342 (2011).
64. Jahn, R., Schiebler, W., Ouimet, C. & Greengard, P. A 38,000-dalton membrane protein (p38) present in synaptic vesicles. *Proc. Natl Acad. Sci. USA* **82**, 4137–4141 (1985).
65. Bohil, A. B., Robertson, B. W. & Cheney, R. E. Myosin-X is a molecular motor that functions in filopodia formation. *Proc. Natl Acad. Sci. USA* **103**, 12411–12416 (2006).
66. Cohen, L. S. & Studzinski, G. P. Correlation between cell enlargement and nucleic acid and protein content of hela cells in unbalanced growth produced by inhibitors of DNA synthesis. *J. Cell. Physiol.* **69**, 331–339 (1967).
67. Krombach, F. et al. Cell size of alveolar macrophages: an interspecies comparison. *Environ. Health Perspect.* **105**, 1261–1263 (1997).
68. Luby-Phelps, K. Cytoarchitecture and physical properties of cytoplasm: volume, viscosity, diffusion, intracellular surface area. *Int. Rev. Cytol.* **192**, 189–221 (2000).
69. Puck, T. T., Marcus, P. I. & Cieciura, S. J. Clonal growth of mammalian cells in vitro; growth characteristics of colonies from single HeLa cells with and without a feeder layer. *J. Exp. Med.* **103**, 273–283 (1956).
70. Zhao, L. et al. Intracellular water-specific MR of microbead-adherent cells: the HeLa cell intracellular water exchange lifetime. *NMR Biomed.* **21**, 159–164 (2008).
71. Philips, R., Kodev, J., Therio, J. & Garcia, H. *Physical Biology of the Cell* (Garland Science, 2008).
72. Zou, M., Holloway, M., Carr, N. & Ju, T. Topology-constrained surface reconstruction from cross-sections. *ACM Trans. Graph.* https://doi.org/10.1145/2766976 (2015).
73. Roy, A., Kucukural, A. & Zhang, Y. I-TASSER: A unified platform for automated protein structure and function prediction. *Nat. Protoc.* https://doi.org/10.1038/nprot.2010.5 (2010).
74. Zhang, Y. I-TASSER server for protein 3D structure prediction. *BMC Bioinformatics* https://doi.org/10.1186/1471-2105-9-40 (2008).

Acknowledgements

We thank J. Lovric and M. von Elling-Tamen for help with the immunostaining experiments, as well as N. Hartelt and C. Schäfer for expert technical assistance. We thank N. Brose (Göttingen, Germany), V. Haucke (Berlin, Germany), R. Jahn (Göttingen, Germany), P. Jonas (Klosterneuburg, Austria) and V. Nägerl (Bordeaux, France) for advice on the initial manuscript. We would also like to thank E. Fornasiero for many fruitful discussions and comments on the manuscript. The work was supported by a grant to S.O.R. from the Deutsche Forschungsgemeinschaft (DFG; SFB1286/A3, RI 1967/11-1, RI 1967/10-1/NeuroNex; SFB1190/P09, and under Germany's Excellence Strategy - EXC 2067/1-390729940), by a grant to S.O.R. from Nieders Vorab (76251-12-6/19/ZN 3458), by a grant to S.O.R. from the German Ministry for Education and Research (13N15328/NG-FLIM), as well as by a grant to H.U. from the DFG (SFB1286/A8), and by a grant to T.S. (NIH grant R15NS095318).

Author contributions

M.S.H. performed most of the fluorescence imaging experiments and the biochemistry experiments. T.M.D. developed software for data analysis and performed several

fluorescence imaging experiments. S.J. also performed several fluorescence imaging experiments. T.S. performed all EM experiments (which were analyzed by V.S. and C.K.). S.M. and H.U. designed and performed all MS experiments. R.L. performed clustering analysis for Extended Data Fig. 3e,f. B.R. generated the synapse models. S.O.R. and M.S.H. designed the experiments and analyzed most of the data. All authors contributed to writing the manuscript.

Competing interests

The authors declare no competing interests.

Additional information

Extended data is available for this paper at https://doi.org/10.1038/s41593-021-00874-w.

Supplementary information The online version contains supplementary material available at https://doi.org/10.1038/s41593-021-00874-w.

Correspondence and requests for materials should be addressed to S.O.R.

Peer review Information *Nature Neuroscience* thanks the anonymous reviewers for their contribution to the peer review of this work.

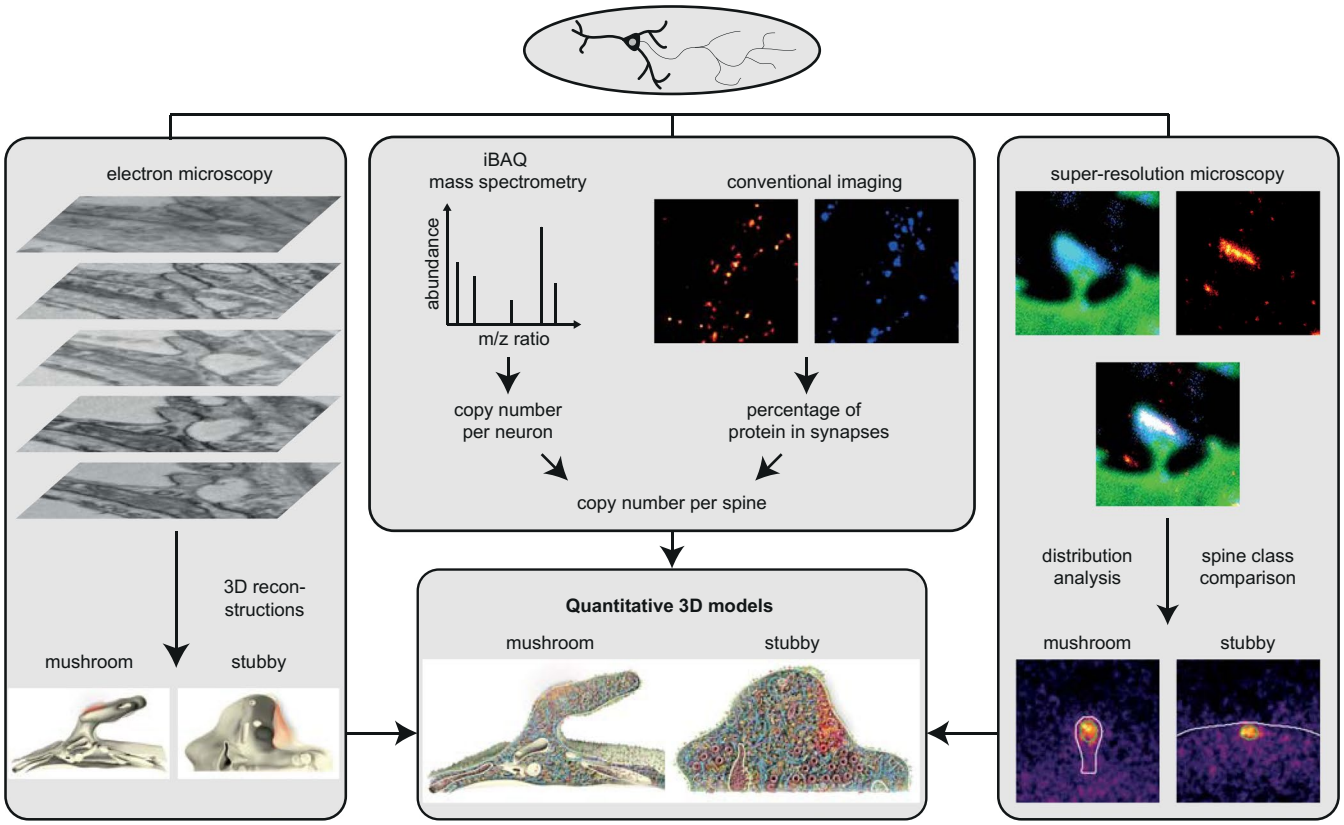

Extended Data Fig. 1 | An integrative approach to analyze dendritic spines quantitatively. We used serial-section electron microscopy (left panel) to determine the shapes, volumes and organelle distributions of the spines, and to generate the basic scaffold of 3D spines. We then used mass spectrometry to measure the neuronal protein copy numbers (top center panel), and we combined this with fluorescence microscopy, for every protein target, to obtain the copy numbers per spine. We also used super-resolution STED microscopy to determine the average location of the proteins, in tens of thousands of expert-annotated synapses (right panel). We then combined all of the information obtained with knowledge from more than 400 publications, to generate quantitative 3D models of average stubby and mushroom spines (bottom center panel).

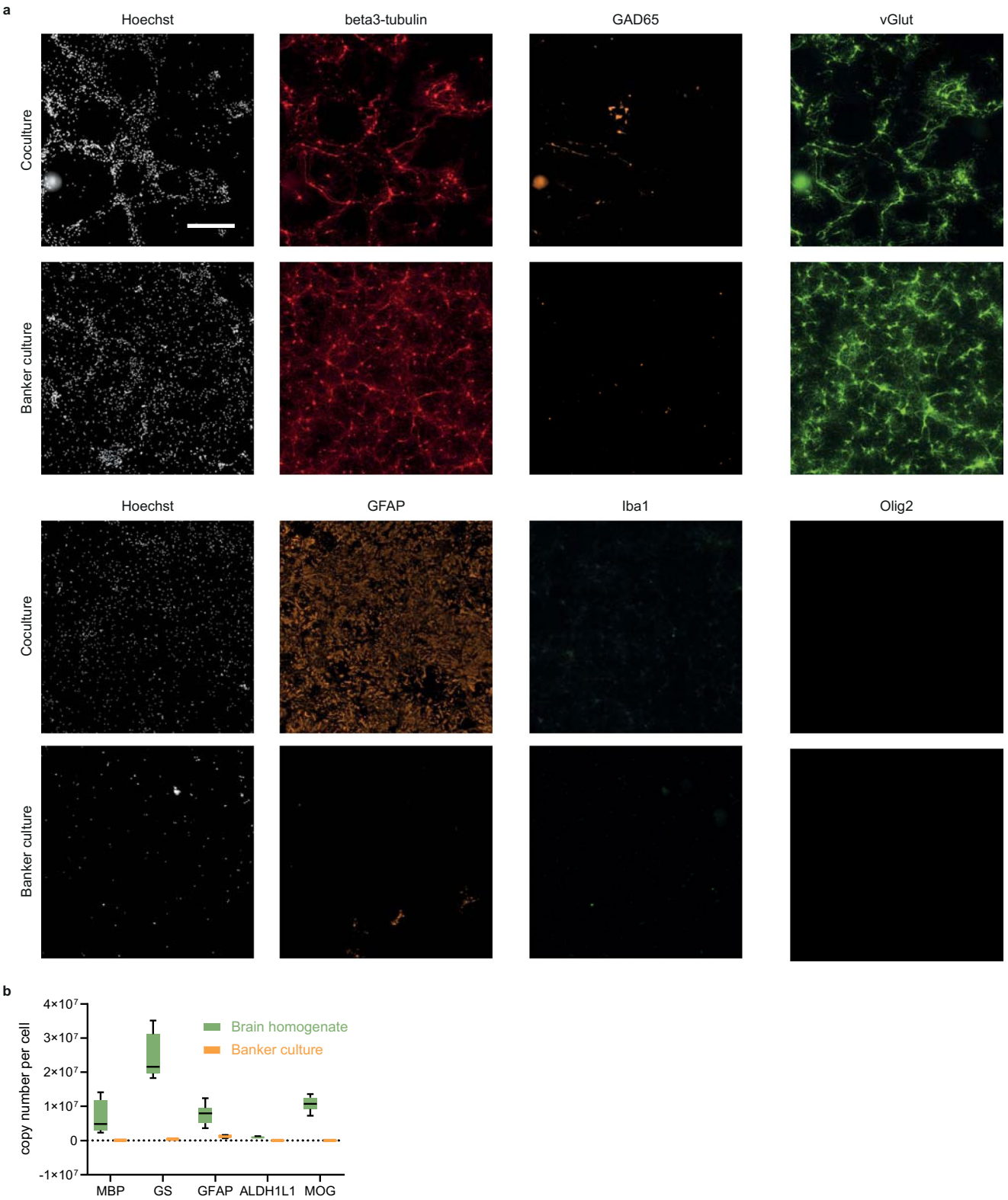

Extended Data Fig. 2 | See next page for caption.

Extended Data Fig. 2 | Banker cultures are a good model for analyzing neuronal proteins. a, Top rows: Banker cultures or neuron-glia co-cultures were immunostained for the neuronal marker β3-tubulin, for the GABAergic neuron marker glutamate decarboxylase (GAD65), for the glutamatergic neuron marker vGlut (vesicular glutamate transporter). Bottom rows: the cells were immunostained for the astrocyte marker glial fibrillary acidic protein (GFAP), for the microglia marker ionized calcium binding adaptor molecule 1 (Iba1), and for the oligodendrocyte marker oligodendrocyte transcription factor 2 (Olig2). Glutamatergic neurons represent the wide majority of the cells in the Banker cultures, with few other cell types present. Scale bar = 500 μm. **b**, An analysis of the protein copy numbers per cell, for different non-neuronal markers: myelin basic protein (MPB, myelin marker), glutamine synthetase (GS, astrocyte marker), GFAP, 10-Formyltetrahydrofolate Dehydrogenase (ALDH1L1, astrocyte marker), and myelin-oligodendrocyte glycoprotein (MOG, oligodendrocyte marker). The values were obtained in mass spectrometry analyses of Banker cultures (n = 4 experiments) or of rat brain homogenates (n = 8 experiments). The non-neuronal markers are virtually absent in Banker cultures. Whiskers show minimum and maximum values, the box shows quartiles and median.

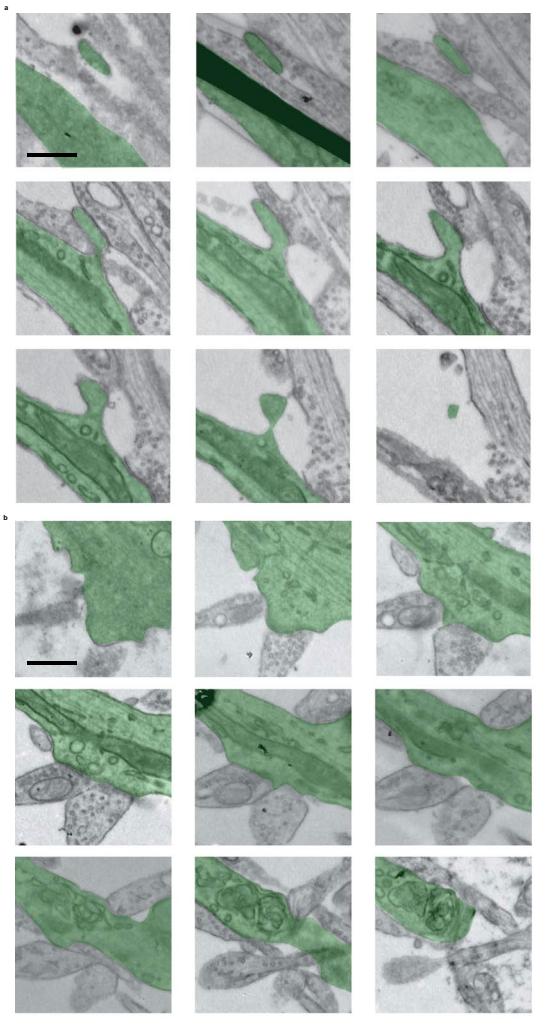

c

Parameter	PSD Area (µm²)	Surface Area (µm²)	% PSD of Surface Area	Volume (µm³)	Number of vesicles	Number of vacuoles	Vacuole volume (µm³)	Mitochondria volume (µm³)
Mushroom	0.106 ± 0.066	1.513 ± 0.743	6.6 ± 1.4	0.189 ± 0.158	10.167 ± 15.013	1.067 ± 1.552	1.088 ± 2.102	1.502 ± 2.985
Stubby	0.142 ± 0.090	1.387 ± 0.509	9.2 ± 3.2	0.179 ± 0.109	6.882 ± 12.526	1.559 ± 2.402	1.139 ± 1.959	2.575 ± 6.221

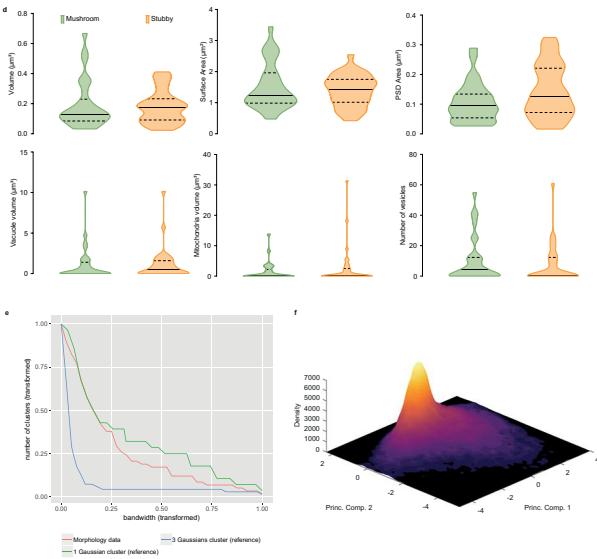

Extended Data Fig. 3 | See next page for caption.

Extended Data Fig. 3 | Electron microscopy characterization of dendritic spines in hippocampal cultures, and Gauss shift clustering of spine morphological parameters. a. Nine consecutive sections of a mushroom spine. Scale bar = 500 nm. **b**, Nine consecutive sections of a stubby spine. Scale bar = 500 nm. **c**, Average parameters obtained from 3D reconstructions of 30 mushroom spines and 34 stubby spines. The values show means ± SEM. **d**, The different panels show the total spine volume, spine surface area, PSD area, mitochondria volume, vacuole volume, and the number of small vesicles for mushroom and stubby spines. No significant differences were found (Kruskal-Wallis test followed by two-sided Dunn's test). Thick lines indicate the median, dashed lines the upper and lower quartile. **e**, We also validated the findings from the EM dataset by comparing a large dataset of spines imaged with fluorescence microscopy. We relied on the lipid dye DiO to label the plasma membrane and to reveal the general morphology of the spines, while the PSD was indicated by an immunostaining for the marker Homer1. We then analyzed the area, height and width of the spine heads, along with the area occupied by the Homer1 signal, the intensity of this signal, and the size of an ellipse fitted on the Homer1 staining. Using these parameters, we could not find significant differences between the two types of spines, asit can be observed that curve of the morphology data is very similar to a 1 Gaussian cluster reference set, in contrast to a 3 Gaussian cluster reference set. Data shown in scale-space. The axes are transformed such that the graphs fit into the same coordinate system. The number of clusters is transformed such that "1.0" refers to the maximum number of clusters for the bandwidth segment we are interested in. The bandwidth is transformed such that the logarithm of the bandwidth lies between 0.0 and 1.0. **f**, Principal component analysis of the morphology data. No subpopulations can be identified. The bandwidth of the Gauss shift clustering is 0.5.

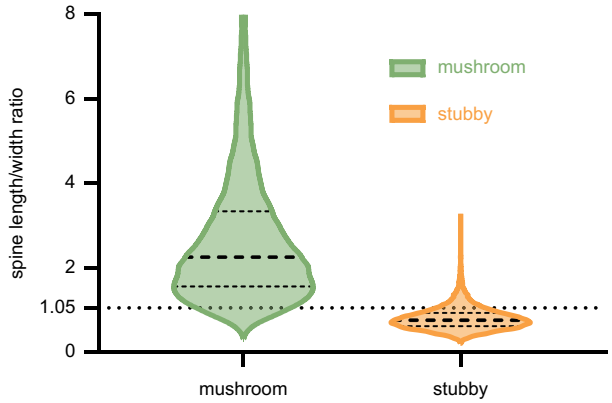

Extended Data Fig. 4 | Post-hoc comparison of spine classification in this study to published criteria for automatic workflows. We have checked our manual classifications of spines post-hoc, based on the criteria laid out in previous publications: (Risher, W. C., Ustunkaya, T., Alvarado, J. S. & Eroglu, C. Rapid golgi analysis method for efficient and unbiased classification of dendritic spines. *PLoS One* 9, (2014); Rodriguez, A., Ehlenberger, D. B., Dickstein, D. L., Hof, P. R. & Wearne, S. L. Automated three-dimensional detection and shape classification of dendritic spines from fluorescence microscopy images. *PLoS One* 3, (2008)), which define the threshold between mushroom and stubby spines as a length to width ratio of 1.05 (mean of criteria from these publications). In line with the published criteria, spines labeled as mushroom in this study exceed the defined length/width ratio (dotted line), whereas the vast majority of stubby spines are below it.

Extended Data Fig. 5 | See next page for caption.

Extended Data Fig. 5 | Detailed description of zone analysis for the STED images of spine proteins. a, We separated the space occupied by spines in different zones, from the PSD area (red) to the dendritic shaft (green). The presence of different proteins in these zones was then analyzed. Scale bar = 500 nm. **b**, To generate 3D models of the spines, we projected the zones into the 3D space of two dendritic reconstructions. We chose two spines whose parameters (described in Extended Data Fig. 3) were closest to the average of all mushroom or, respectively, stubby spines investigated. The zones from panel (**a**) were then assigned in the model voxels, as shown in the graphs. The precise proportions of the zones, as in panel (**a**), were respected in the models. **c**, For modeling purposes, we also assigned different identities to the vacuoles present in these spines, as indicated in the color legend. Scale bar = 500 nm.

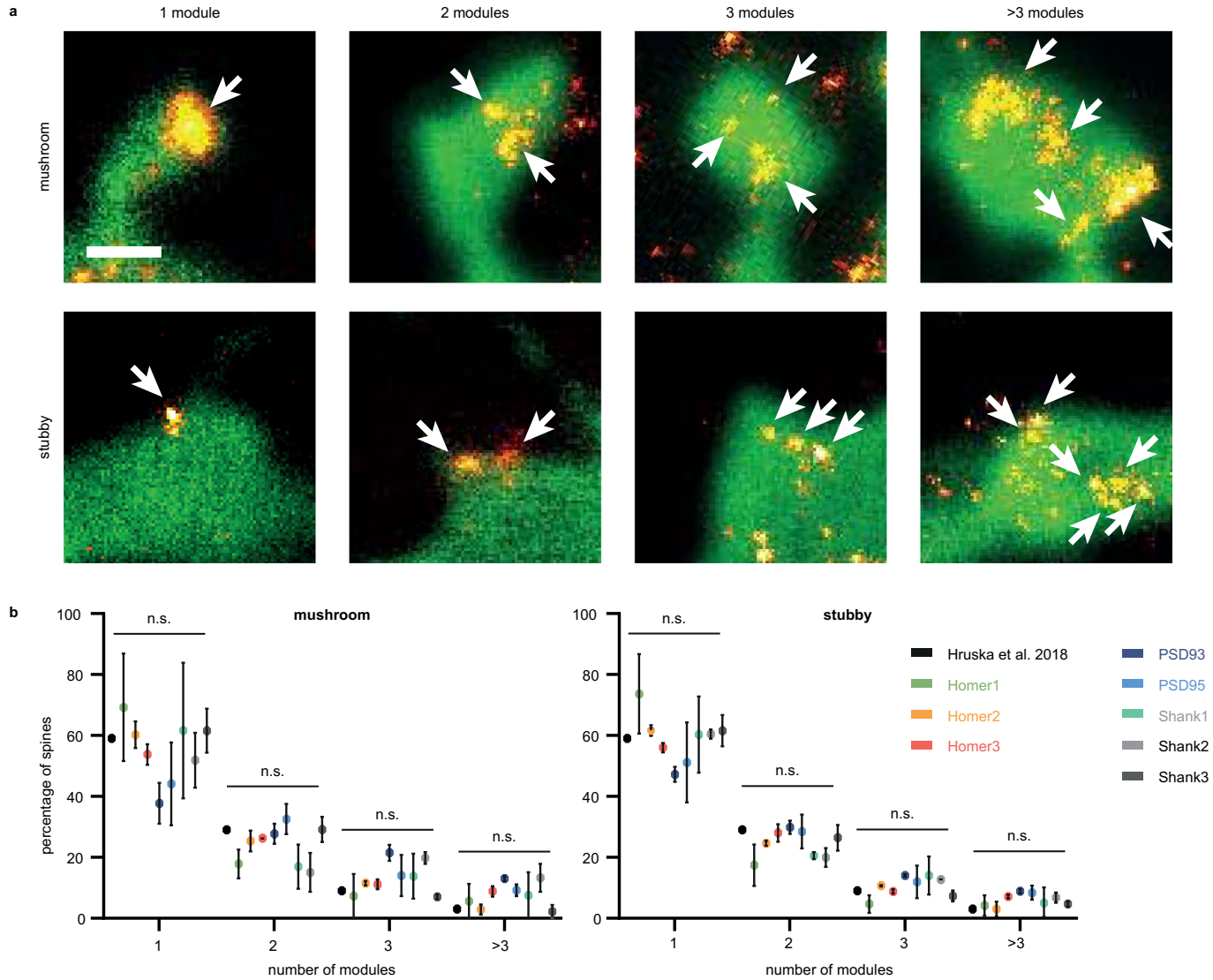

Extended Data Fig. 6 | An analysis of nanomodules in the different spines. a, We analyzed several bona fide PSD proteins, to determine their organization in nanoscale modules. Representative images of nanomodules are shown, the PSD is visualized in red-hot, the membrane in green. Arrows indicate modules, scale bar = 500 nm. The following proteins are shown: Mushroom 1 module – Homer1, 2 modules – Shank3, 3 modules – Shank3, >3 modules – Homer3; Stubby 1 module – Shank1, 2 modules – Shank1, 3 modules – PSD93, >3 modules – PSD95. **b**, As recently demonstrated15, the PSD is separated in two or more nanomodules for approximately 40% of the mushroom spines. Stubby spines showed the same pattern. Bar charts show mean ± SEM. Friedman test followed by two-sided Dunn's tests. For information on sample size for each protein please refer to Supplementary Table 5.

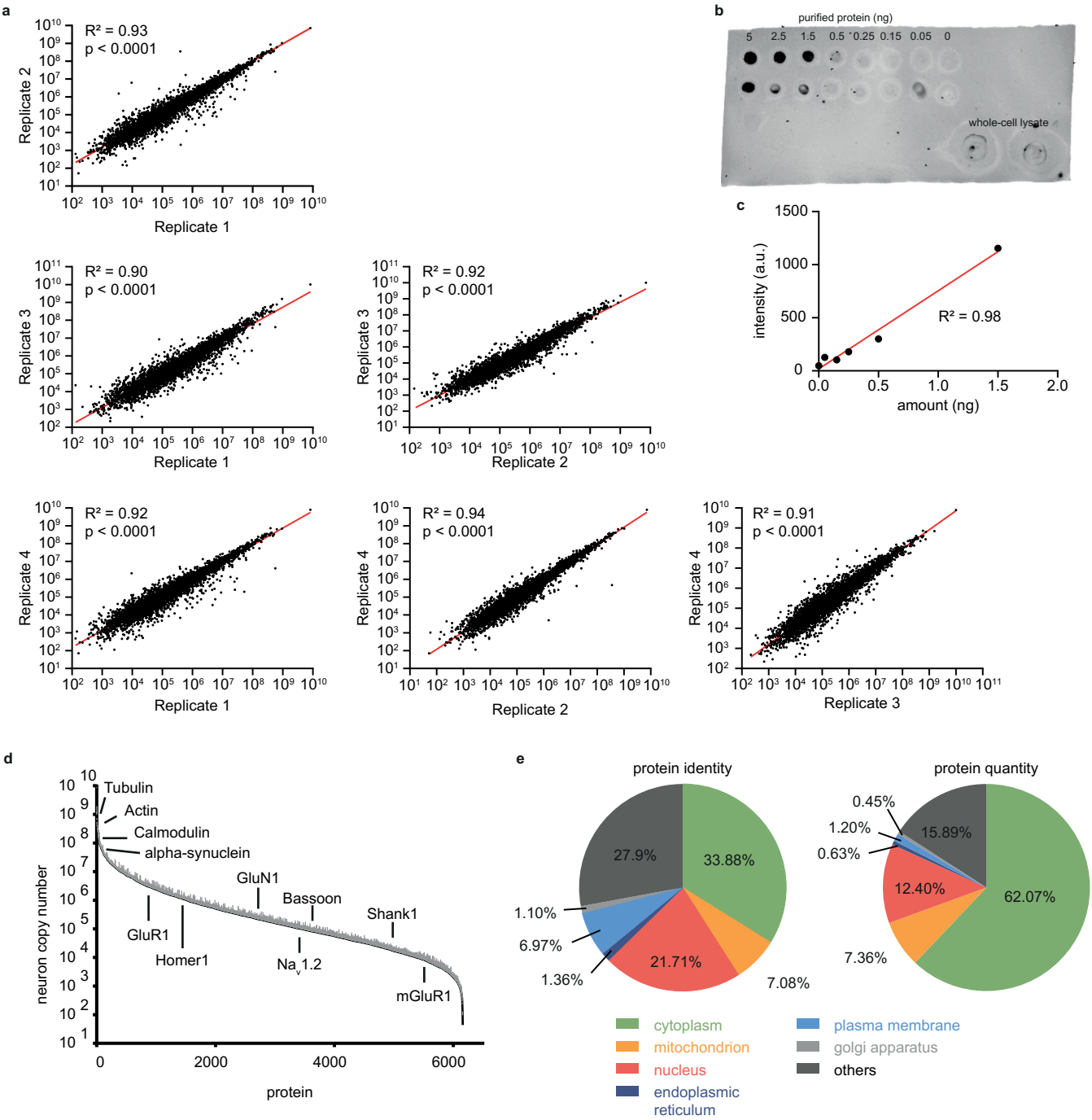

Extended Data Fig. 7 | Technical details on the biochemical analyses of Banker cultures, and an overview of the mass spectrometry results at the neuron level. a, iBAQ mass spectrometry analysis (performed as in 28). The graphs indicate the correlation between results obtained in three different biological replicates (average R2 of 0.99, two-sided F-test). **b**-**c**, Dot blotting. For several proteins (Dopamine Receptor 1, Dopamine Receptor 2, LNGFR, mGluR2, Rapsyn, VAMP2) we employed dot blotting, as indicated in this example Neurogranin). Different amounts of purified proteins were blotted, in parallel with Banker cell lysates (panel **a**). The protein amounts were obtained by linear interpolation on the purified protein amounts (panel **b**). **d**, Over 6000 proteins were identified, in amounts spanning 8 orders of magnitude. **e**, An overview of the organelle distributions of the analyzed proteins. Cytosolic proteins make only one third of the proteins identified, in terms of protein species (identities), but sum to more than 60% of all proteins in terms of amounts.

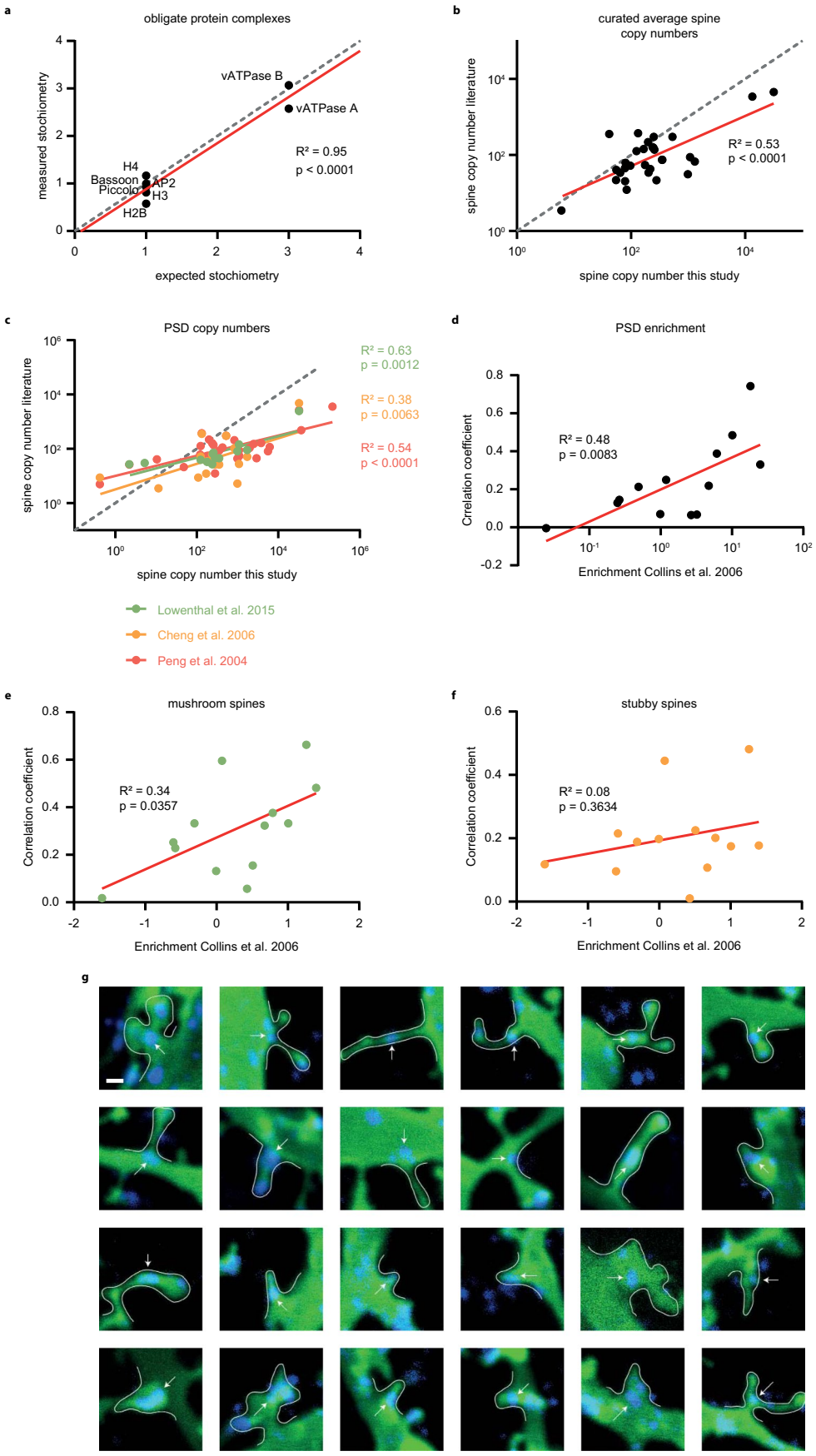

Extended Data Fig. 8 | See next page for caption.

Extended Data Fig. 8 | Comparisons of our protein copy numbers with the literature, and examples of dendritic spines classified as "other". a, To validate our mass spectrometry analysis, we calculated the expected copy numbers for several proteins. First, we calculated the ratio of vATPase A and B subunit copy numbers to vATPase subunit a copies and compared it to its known stoichiometry (Kitagawa et al., 2008). 3 Second, we estimated the copy numbers per neuron of the presynaptic proteins Piccolo and Bassoon, based on their known copy numbers per synapse 2 and the known number of synapses in our preparation (see Extended Data Figure 9), and. we calculated the ratio against the respective measured quantities of Bassoon and Piccolo. Third, we compared the ratio of the core nucleosome subunits to H2A and the ratio of AP2 subunits α and β. The measured copy numbers are very close to the respective estimates (two-sided F-test; compare the linear fit, in red, with the identity line, in gray). **b**, A comparison of the copy numbers for 28 proteins (two-sided F-test) that had previously been estimated in the literature[4] as well as: Antal, M. *et al*. Numbers, densities, and colocalization of AMPA- and NMDA-type glutamate receptors at individual synapses in the superficial spinal dorsal horn of rats. *J. Neurosci*. 28, 9692–701 (2008). Cheng, D. *et al*. Relative and absolute quantification of postsynaptic density proteome isolated from rat forebrain and cerebellum. *Mol. Cell. Proteomics* 5, 1158–70 (2006). Lowenthal, M. S., Markey, S. P. & Dosemeci, A. Quantitative Mass Spectrometry Measurements Reveal Stoichiometry of Principal Postsynaptic Density Proteins. *J. Proteome Res*. 150415143859000 (2015) doi:10.1021/acs.jproteome.5b00109. Masugi-Tokita, M. *et al*. Number and density of AMPA receptors in individual synapses in the rat cerebellum as revealed by SDS-digested freeze-fracture replica labeling. *J. Neurosci*. 27, 2135–44 (2007). Nair, D. *et al*. Super-resolution imaging reveals that AMPA receptors inside synapses are dynamically organized in nanodomains regulated by PSD95. *J. Neurosci*. 33, 13204–24 (2013). Nusser, Z. *et al*. Cell type and pathway dependence of synaptic AMPA receptor number and variability in the hippocampus. *Neuron* 21, 545–559 (1998). Otmakhov, N. & Lisman, J. Measuring CaMKII concentration in dendritic spines. *J. Neurosci. Methods* 203, 106–114 (2012). Peng, J. *et al*. Semiquantitative proteomic analysis of rat forebrain postsynaptic density fractions by mass spectrometry- Supplement. *J. Biol. Chem*. (2004). **c**, Comparisons for the same proteins (two-sided F-test), measured in three individual studies: Cheng, D. *et al*. Relative and absolute quantification of postsynaptic density proteome isolated from rat forebrain and cerebellum. *Mol. Cell. Proteomics* 5, 1158–70 (2006). Peng, J. *et al*. Semiquantitative proteomic analysis of rat forebrain postsynaptic density fractions by mass spectrometry- Supplement. *J. Biol. Chem*. (2004). Lowenthal, M. S., Markey, S. P. & Dosemeci, A. Quantitative Mass Spectrometry Measurements Reveal Stoichiometry of Principal Postsynaptic Density Proteins. *J. Proteome Res*. 150415143859000 (2015) doi:10.1021/acs.jproteome.5b00109. **d**-**f**, A comparison of the enrichment in the PSD of several proteins analyzed in STED microscopy in this study, and in Western Blot investigations of isolated PSDs in the study of 34. Panel (**d**) shows an analysis across all spines, irrespective of class; panel (**e**) shows mushroom spines, while panel (**f**) shows stubby spines. Overall, the biochemically-derived enrichment in the PSD correlates well with the enrichment observed by super-resolution microscopy. This relation is significant when mushroom spines are analyzed in isolation but is not significant for stubby spines (two-sided F-test). A possible conclusion is that stubby spines are less well controlled than mushroom spines (see also Fig. 5). **g**, During image analysis, we sometimes observed strong Homer1 (blue) staining without a clear mushroom or stubby shaped spine (membrane stained with DiO, green). These synapses were classified as "others". Several representative images are shown. Note the diverse morphology. Scale bar = 500 nm.

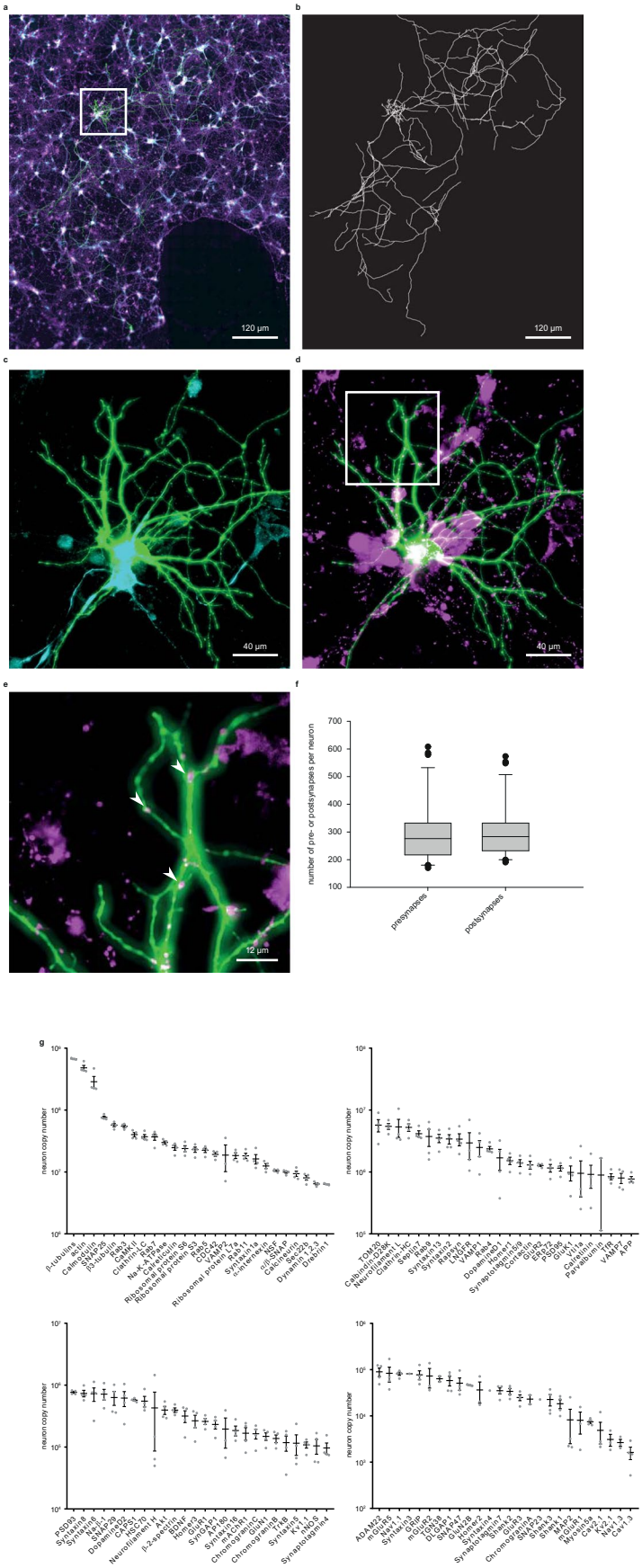

Extended Data Fig. 9 | See next page for caption.

Extended Data Fig. 9 | An analysis of the number of synapses in cultured neurons. a, Individual neurons were labeled fluorescently by overexpressing a membrane-bound GFP molecule (EGFP coupled to the palmitoylation domain of GAP43), which spreads to all neurites. Single neurons were then visualized (green). Two other color channels were used for immunostainings of synaptophysin (magenta), to reveal synaptic boutons, and for Ankyrin G (cyan), to reveal the axonal initial segments, and thereby to differentiate between dendrites and axonal branches. The boxed area is shown in panel **c**-**d**. **b**, Manual tracing of neurites, to identify all of the neurites of the labeled neuron (both axonal and dendritic). **c**, A high-zoom view, to enable the identification of the axon, labeled by Ankyrin G (cyan, arrowhead). The cyan signal to the lower left is due to staining in an adjoining neuron, not to staining in the green-labeled neuron. **d**, The same view, for the synaptophysin (magenta) channel. **e**, A higher-zoom view of the region boxed in panel **d**, which enables the visualization of synapses, consisting of synaptophysin-labeled boutons (magenta) closely apposed to GFP-labeled dendrites (green). Three examples are shown by arrowheads. Similarly, the number of presynapses was estimated by counting the number of synaptophysin-labeled boutons within the GFP-labeled axons. **f**, The number of pre- or postsynapses, shown as a box plot. The average values are 294 presynapses per neuron and 299 postsynapses per neuron, from 33 analyzed neurons, in 6 independent experiments. Box plots show the following: mid-line = median; boxes = 50th percentile; error bars = 75th percentile; symbols = outliers. Scale bars: 120 μm for panels **a**-**b**, 40 μm for panels **c**-**d**, 12 μm for panel e. **g**, Variation in the copy numbers of spine proteins. The graphs indicate the copy numbers of the proteins we analyzed in detail in the rest of the manuscript. The values are shown per neuron, from 4 independent experiments. Each dot show from one experiment, the lines indicate mean ± SEM.

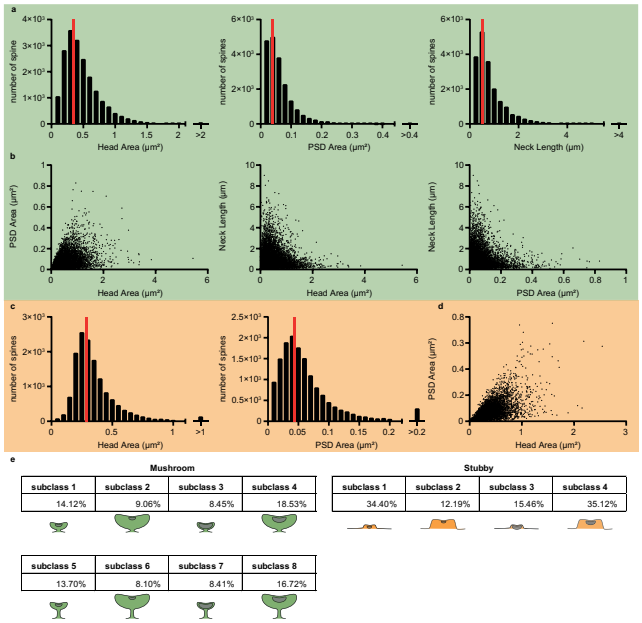

e

Mushroom

subclass 1	subclass 2	subclass 3	subclass 4
14.12%	9.06%	8.45%	18.53%

subclass 5	subclass 6	subclass 7	subclass 8
13.70%	8.10%	8.41%	16.72%

Stubby

subclass 1	subclass 2	subclass 3	subclass 4
34.40%	12.19%	15.46%	35.12%

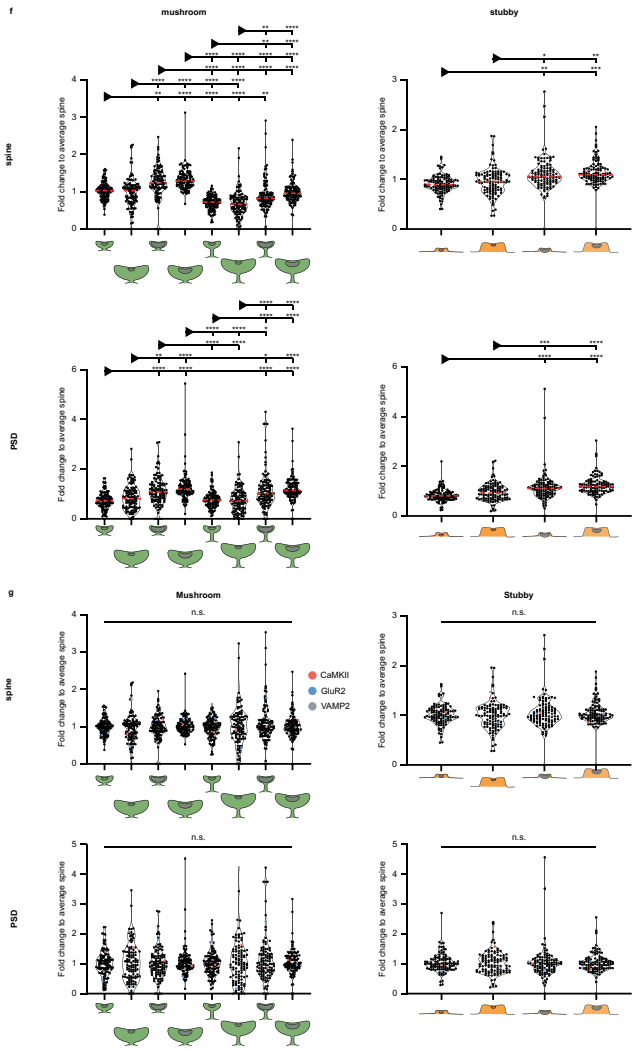

Extended Data Fig. 10 | Analyzing spine subclasses reveals no striking differences. a, Mushroom spines were grouped into subclasses, based on head size, PSD size and neck length, using the median of the respective distributions as borders (red line). **b**, Scattering the different parameters against each other does not reveal obvious subpopulations. **c**, Stubby spines were grouped based on head and PSD size, again using the median of the respective distributions (red line). **d**, Scattering did not reveal obvious subpopulations. **e**, The percentages of spines in each subclass are shown. No subclasses show extremely high or low occupancy. **f**, We measured the intensity of each protein for each subclass, as a proxy of its abundance in the respective subclasses. We then divided the values by the overall intensity of the respective protein (averaged across all spines). This provides the relative abundance of each protein, in each spine subclass. The top panels show this analysis for the protein abundance in the whole volume of the spines, while the bottom panels show the analysis for the protein abundance in the PSD area. The dashed lines indicate the medians. We compared the protein abundance values between subclasses and found many significant differences. (Kruskal-Wallis followed by two-sided Dunn's tests). For mushroom spines, the protein abundance across the whole spine is lower in spines exhibiting a long neck, and appears to be larger in spines with large PSDs. When only considering abundance in the PSD, the neck length no longer has a strong effect. The size of the PSD, as expected, correlates with protein abundance in the PSD. In stubby spines, a larger PSD also correlates with higher protein abundance, both in the whole spine volume and in the PSD. Head size does not affect protein abundance in either analysis. **g**, We then asked whether individual proteins tend to be significantly more abundant in particular spine subclasses. For this, we normalized protein abundances in each subclass by dividing the results from panel (**f**) by the median values of each subclass. As expected, this normalization removes any significant differences between the subclasses as a whole (Kruskal-Wallis followed by Dunn's tests). However, now we could analyze each protein individually across subclasses, to test whether individual proteins are particularly abundant in the respective subclasses, independent of the overall effects induced by the morphology or the size of the respective subclasses. We found only extremely few differences. The results can be found in Supplementary Table 3 (two-sided Mann-Whitney U tests followed by Bonferroni correction).

nature research

Corresponding author(s): Silvio Rizzoli

Last updated by author(s): Apr 14, 2021

Reporting Summary

Nature Research wishes to improve the reproducibility of the work that we publish. This form provides structure for consistency and transparency in reporting. For further information on Nature Research policies, see our Editorial Policies and the Editorial Policy Checklist.

Statistics

For all statistical analyses, confirm that the following items are present in the figure legend, table legend, main text, or Methods section.

n/a	Confirmed
☐	☒ The exact sample size (*n*) for each experimental group/condition, given as a discrete number and unit of measurement
☐	☒ A statement on whether measurements were taken from distinct samples or whether the same sample was measured repeatedly
☐	☒ The statistical test(s) used AND whether they are one- or two-sided *Only common tests should be described solely by name; describe more complex techniques in the Methods section.*
☐	☒ A description of all covariates tested
☐	☒ A description of any assumptions or corrections, such as tests of normality and adjustment for multiple comparisons
☐	☒ A full description of the statistical parameters including central tendency (e.g. means) or other basic estimates (e.g. regression coefficient) AND variation (e.g. standard deviation) or associated estimates of uncertainty (e.g. confidence intervals)
☐	☒ For null hypothesis testing, the test statistic (e.g. *F*, *t*, *r*) with confidence intervals, effect sizes, degrees of freedom and *P* value noted *Give P values as exact values whenever suitable.*
☒	☐ For Bayesian analysis, information on the choice of priors and Markov chain Monte Carlo settings
☐	☒ For hierarchical and complex designs, identification of the appropriate level for tests and full reporting of outcomes
☐	☒ Estimates of effect sizes (e.g. Cohen's *d*, Pearson's *r*), indicating how they were calculated

Our web collection on statistics for biologists contains articles on many of the points above.

Software and code

Policy information about availability of computer code

Data collection	Data was acquired using Leica Application Suite Advanced Fluorescence 2.7.3.9723 and NIS Elements 5.02.03
Data analysis	Custom code written in Matlab2017b and 2019b, Python 3.7.6, icy 1.9.5.1, Graphpad Prism 8 and Excel 2016 was used in this study. Mass spectrometry analysis was performed using MaxQuant 1.5.3.8 or 1.6.0.16.

For manuscripts utilizing custom algorithms or software that are central to the research but not yet described in published literature, software must be made available to editors and reviewers. We strongly encourage code deposition in a community repository (e.g. GitHub). See the Nature Research guidelines for submitting code & software for further information.

Data

Policy information about availability of data

All manuscripts must include a data availability statement. This statement should provide the following information, where applicable:

- Accession codes, unique identifiers, or web links for publicly available datasets
- A list of figures that have associated raw data
- A description of any restrictions on data availability

The mass spectrometry proteomics data have been deposited to the ProteomeXchange Consortium via the PRIDE partner repository with the dataset identifier PXD015308. Image data are available from the corresponding author on reasonable request.

Field-specific reporting

Please select the one below that is the best fit for your research. If you are not sure, read the appropriate sections before making your selection.

☒ Life sciences ☐ Behavioural & social sciences ☐ Ecological, evolutionary & environmental sciences

For a reference copy of the document with all sections, see nature.com/documents/nr-reporting-summary-flat.pdf

Life sciences study design

All studies must disclose on these points even when the disclosure is negative.

Sample size	The largest possible numbers of experiments were performed, taking into account the high number of target proteins (>100), and is well within the range of typical super-resolution imaging experiments. No formal sample size calculation was performed, as this would require an estimate of the effect size between two conditions, whereas we are only investigated a single condition here.
Data exclusions	No data were excluded
Replication	In general 3 independent experiments were performed, with several hundred synapses investigated per protein. All replications were successful. For a detailed list see Supplementary Table 4, for an example analysis please see Extended Data Figure 6.
Randomization	Not relevant for this manuscript, as only 1 experimental group was investigated.
Blinding	Blinding was not relevant to the study, because no conditions were compared, only 1 experimental group was investigated.

Reporting for specific materials, systems and methods

We require information from authors about some types of materials, experimental systems and methods used in many studies. Here, indicate whether each material, system or method listed is relevant to your study. If you are not sure if a list item applies to your research, read the appropriate section before selecting a response.

Materials & experimental systems

n/a	Involved in the study
☐	☒ Antibodies
☒	☐ Eukaryotic cell lines
☒	☐ Palaeontology and archaeology
☐	☒ Animals and other organisms
☒	☐ Human research participants
☒	☐ Clinical data
☒	☐ Dual use research of concern

Methods

n/a	Involved in the study
☒	☐ ChIP-seq
☒	☐ Flow cytometry
☒	☐ MRI-based neuroimaging

Antibodies

Antibodies used	Please refer to the relevant part of the Methods, describing at length all antibodies
Validation	ADAM22 mouse 500 Novus Biologicals NBP2-22425 Validated in 21 Akt (pan) rabbit 400 Cell Signaling 4691 Validated in 37 α/β-SNAP mouse 100 Jahn Laboratory 77.2 Validated in 23 α-internexin rabbit 500 LSBio LS-B10413 Clear observation of internexin filaments, as expected from the literature. Low signal outside of filaments. Shown in Supplementary Data File 1. AP180 rabbit 100 Synaptic Systems 155 003 K.O. validated Ankyrin-G mouse 500 Neuromab AB_10673030, clone N106/36 Validated in 115 APP mouse 100 Millipore MAB-348 Validated in 23 Arc rabbit 1000 Synaptic Systems 156 003 K.O. validated β-2-spectrin mouse 100 BDBiosciences 612562 Validated in 14 β-tubulin llama 100 Self-made See 38 Validated in 38

β-3-Tubulin rabbit 500 Cell Signaling 5568 Validated in 39

BDNF rabbit 100 Biorbyt orb38809 Manufacturer, available at antibodypedia.com

Calbindin-D28K rabbit 500 Synaptic Systems 214 002 Control Antigen

Calcineurin A rabbit 1000 Synaptic Systems 387 002 Control Antigen

Calmodulin rabbit 100 Abcam ab45689 Validated in 23

Calreticulin rabbit 200 Cell Signaling 12238 Validated in 14

Calretinin rabbit 250 Novus Biologicals NBP1-88220 K.D. validated

CaMKII (alpha subunit, phosphorylated form) mouse 500 Abnova MAB6627 Validated in 40

CAPS1 rabbit 500 Abcam ab69797 Validated in 23

Cav1.3 rabbit 50 Alomone Labs ACC-311 Control Antigen

Cav2.1 rabbit 500 Synaptic Systems 152 203 K.O. validated

CDC42 rabbit 100 Thermo Scientific PA1-092 K.D. validated 41

Chromogranin A rabbit 500 Synaptic Systems 259 003 K.O. validated

Chromogranin B rabbit 500 Synaptic Systems 259 103 K.O. validated

Chromogranin C rabbit 250 Abcam ab12241 Validated in 42

Clathrin heavy chain mouse 100 BD Biosciences 610499 Validated in 23

Clathrin light chain mouse 1000 Synaptic Systems 113 011 Validated in 23

Cortactin mouse 500 Synaptic Systems 313 111 Validated in 43

DLGAP1 rabbit 50 Novus Biologicals NBP1-76911 Validated in 21

Dopamine receptor 1 rabbit 1000 Abcam ab40653 Control antigen

Dopamine receptor 2 rabbit 500 Merck AB5084P K.O. validated in 44

Drebrin1 mouse 100 Novus Biologicals NB100-1951 Validated in 45

Dynamin 1/2/3 mouse 100 BDBiosciences 610245 Validated in 23

ERp72 rabbit 100 Cell Signaling 5033 Validated in 21

GAD65 mouse 500 Synaptic Systems 198 111 Control antigen

GFAP mouse 500 Synaptic Systems 173 011 Control antigen

GluK1 rabbit 100 Alomone AGC-008 Control antigen

GluN1 mouse 1000 Synaptic Systems 114 011 Validated in 46

GluN2A mouse 100 NeuroMab 75-288 Validated in 21

GluN2B mouse 100 NeuroMab 75-101 Validated in 21

GluR1 rabbit 500 Synaptic Systems 182 003 K.O. validated

GluR2 rabbit 100 Alomone Labs AGC-005 Control antigen

GluR3 mouse 100 Invitrogen 32-0400 Validated in 21

GRIP1/2 rabbit 100 Synaptic Systems 151 003 Control antigen

Homer1 mouse 500 Synaptic Systems 160 011 Control antigen

Homer1 rabbit 500 Synaptic Systems 160 003 Control antigen

Homer2 rabbit 500 Synaptic Systems 160 203 Validated in 47

Homer3 rabbit 250 Synaptic Systems 160 303 Control antigen

HSC70 mouse 100 Santa Cruz sc-7298 Control antigen

Iba1 guinea pig 500 Synaptic Systems 234 004 Control antigen

IGF-1 Receptor rabbit 300 Cell Signaling 3027 Validated in 21,48

KCNJ2 rabbit 100 Novus Biologicals NBP1-95482 Validated in 21

Kv1.1 rabbit 100 Thermo Scientific PA5-19593 Validated in 21

Kv2.1 rabbit 500 Synaptic Systems 231 002 Control antigen

LNGFR rabbit 1000 Cell Signaling 8238 Validated in 49

m-AChR-1 rabbit 100 Novus Biologicals NBP1-87466 Validated in 50

MAP2 rabbit 1000 Synaptic Systems 188 002 Control antigen

mGluR1α rabbit 250 Abcam ab51314 Validated in 51

mGluR2 rabbit 100 Abcam ab150387 Validated in 52

mGluR5 rabbit 100 Abcam ab76316 Validated in 53

myosin5a rabbit 200 Sigma-Aldrich M5062 Validated in 21

Na β 1 rabbit 50 Alomone Labs ASC-041 Control antigen

Na+/K+ ATPase mouse 1000 Thermo Scientific MA3-915 Validated in 21

Nav1.1 rabbit 100 Merck 06-811 Validated in 54

Nav1.3 rabbit 250 Alomone Labs ASC-004 Control antigen

Neurofilament H rabbit 1000 LSBio LS-C143052 Clear observation of filaments, as expected from the

literature. Shown in Supplementary Data File 1. Similar pattern to Neurofilament L. Similar STED fluorescence pattern to multiple previous STED publications 55,56

Neurofilament L rabbit 500 Synaptic Systems 171 002 Validated in 14

nNOS rabbit 100 Thermo Scientific PA1-033 Validated in 21

NSF rabbit 500 Synaptic Systems 123 002 Validated in 23

Olig2 rabbit 500 Synaptic Systems 292 003 Presence only in subset of cells with oligodendrocyte morphology. Missing in all other cells. Data analyzed in Extended Data Fig. 2.

Parvalbumin rabbit 500 Swant PV25 K.O. validated

PSD93 rabbit 300 Invitrogen 34-4700 Validated in 57

PSD95 rabbit 100 Cell Signaling 3450 Validated in 14

Rab11 rabbit 100 Cell Signaling 3539 Validated in 21

Rab3 mouse 100 BD Biosciences 610379 Validated in 23

Rab4 mouse 100 BD Biosciences 610888 Validated in 58

Rab5 mouse 100 Jahn Laboratory cl. 621.3 Validated in 21

Rab7 rabbit 100 Cell Signaling 9367 Validated in 21

Rab9 rabbit 100 Cell Signaling 5118 Validated in 59–61

Rapsyn rabbit 100 Atlas Antibodies HPA039475 Validated in 21

Ribosomal protein L7a rabbit 100 Cell Signaling 2403 Validated in 62

Ribosomal protein S3 rabbit 50 Cell Signaling 9538 Validated in 63

Ribosomal protein S6 rabbit 100 Cell Signaling 2217 Validated in 64

Sec22b rabbit 100 Synaptic Systems 186 003 K.D. validated

Septin7 rabbit 50 Atlas Antibodies HPA029524 Validated in 21

Shank1 rabbit 500 Synaptic Systems 162 013 K.O. validated

Shank2 rabbit 500 Synaptic Systems 162 202 K.O. validated

Shank3 rabbit 500 Synaptic Systems 162 302 K.O. validated

SMI310 mouse 200 Abcam 24570 Validated in 65

SNAP29 rabbit 500 Synaptic Systems 111 302 K.O. validated

SNAP47 rabbit 200 Synaptic Systems 111 403 Validated in 21

SNAP23 rabbit 100 Synaptic Systems 111 202 K.O. validated

SNAP25 mouse 100 Synaptic Systems 111 011 K.O. validated

Synaptophysin guinea pig 1000 Synaptic Systems 101 004 Control antigen

Synaptotagmin4 rabbit 1000 Synaptic Systems 105 143 K.O. validated

Synaptotagmin5/9 rabbit 100 Synaptic Systems 105 053 K.O. validated

Synaptotagmin7 rabbit 250 Synaptic Systems 105 173 K.O. validated

SynGAP1 rabbit 1000 Thermo Scientific PA1-046 Validated in 21

Syntaxin1 mouse 200 Synaptic Systems 110 011 Control antigen

Syntaxin13 mouse 100 Jahn Laboratory cl. 151.1 Validated in 23

Syntaxin16 rabbit 100 Synaptic Systems 110 162 Control antigen

Syntaxin2 rabbit 100 Synaptic Systems 110 022 Control antigen

Syntaxin3 rabbit 100 Synaptic Systems 110 033 Control antigen

Syntaxin4 rabbit 100 Synaptic Systems 110 042 Control antigen

Syntaxin5 rabbit 100 Synaptic Systems 110 053 K.D. validated

Syntaxin6 rabbit 100 Cell Signaling 2869 Validated in 21

Syntaxin8 rabbit 100 Synaptic Systems 110 083 Control antigen

TGN38 rabbit 100 Sigma-Aldrich T9826 Validated in 66

TOM20 mouse 200 Sigma-Aldrich WH0009804M1 Validated in 21

Transferrin Receptor rabbit 100 Abcam ab84036 Validated in 67

TrkB rabbit 500 Abcam ab33655 Validated in 68

vAChT rabbit 100 Synaptic Systems 139 103 K.O. validated

Vamp1 rabbit 500 Synaptic Systems 104 002 Control antigen

Vamp2 mouse 1000 Synaptic Systems 104 211 K.O. validated

VAMP7 rabbit 100 Abcam ab68776 Validated in 21

Vti1a mouse 100 BDBiosciences 611220 Validated in 23

Animals and other organisms

Policy information about studies involving animals; ARRIVE guidelines recommended for reporting animal research

Laboratory animals	Rattus norvegicus, Wistar, both sexes, E18-P0
Wild animals	None
Field-collected samples	None

Ethics oversight	Lower Saxony State Office for Consumer Protection and Food Safety (Niedersächsisches Landesamt für Verbraucherschutz und Lebensmittelsicherheit).

Note that full information on the approval of the study protocol must also be provided in the manuscript.